Properties of Mars' Dayside Low-Altitude Induced Magnetic Field and Comparisons with Venus

Susanne Byrd[1], Zachary Girazian[1], Suranga Ruhunusiri[2]

[1]Department of Physics and Astronomy, University of Iowa, Iowa City, IA
[2]Laboratory for Atmospheric and Space Physics, University of Colorado, Boulder, Boulder, CO, USA

Key Points:

- Unlike Venus, the induced magnetic field profiles at Mars are unable to be categorized into magnetized and unmagentized states.
- At both planets, the solar zenith angle dependence of the induced field strength is controlled by the shape of the magnetic pileup boundary.
- Induced fields at Mars are stronger than expected if assuming the fields form to achieve pressure balance with the oncoming solar wind.

Corresponding author: Susanne Byrd, susbyrd@uiowa.edu

Abstract

Mars and Venus have atmospheres but lack large-scale intrinsic magnetic fields. Consequently, the solar wind interaction at each planet results in the formation of an induced magnetosphere. Our work aims to compare the low-altitude (< 250 km) component of the induced magnetic field at Venus and Mars using observations from Pioneer Venus Orbiter (PVO) and Mars Atmosphere and Volatile EvolutioN (MAVEN). The observations from Mars are restricted to regions of weak crustal magnetism. At Venus, it has long been known the vertical structure of the induced magnetic field profiles have recurring features that enable them to be classified as either magnetized or unmagnetized. We find the induced field profiles at Mars are more varied, lack recurring features, and are unable to be classified in the same way. The solar zenith angle dependence of the low-altitude field strength at both planets is controlled by the shape of the magnetic pileup boundary. Also, because the ionospheric thermal pressure at Venus is often comparable to the solar wind dynamic pressure, the induced fields are weaker than required to balance the solar wind by themselves. By contrast, induced fields at Mars are stronger than required to achieve pressure balance. Lastly, we find the induced fields in the magnetized ionosphere of Venus have a weaker dependence on solar wind dynamic pressure than the induced fields at Mars. Our results point to planetary properties, such as planet-Sun distance, having a major effect on the properties of induced fields at nonmagentized planets.

1 Introduction

A magnetosphere is a region of space around a planetary body where charged particles are deflected by the body's magnetic field. For bodies with active intrinsic field generation, this region is usually large (e.g., ∼10 planetary radii on the sun-facing side for Earth). For bodies without active intrinsic field generation, this region is smaller (< 1 planetary radii) and an induced magnetosphere forms as the magnetic field of the solar wind interacts with the electrically conductive ionosphere (Bertucci et al., 2011). As it encounters the obstacle, an electric current is induced in the ionosphere (Daniell Jr & Cloutier, 1977; Ramstad, 2020). The induced magnetosphere that results from this interaction tends to balance the dynamic pressure from the oncoming solar wind (Luhmann et al., 2004). Typically, an induced field is much weaker than an intrinsic global field. Induced magnetospheres occur on bodies that have an atmosphere but lack a dynamo-generated global magnetic field. Both Venus and Mars fall into this category as unmagentized planets containing atmospheres, and thus both planets have induced magnetospheres. In this paper, we focus on understanding and comparing the structure and variability of the low-altitude (< 250 km) induced magnetic fields of Venus and Mars.

The Pioneer Venus Orbiter (PVO) is the only spacecraft to have consistently measured the low-altitude induced magnetic fields at Venus. Analyses of the PVO data confirmed that Venus has a magnetic field induced solely by interaction with the solar wind (Luhmann & Russell, 1983). They also found most vertical profiles of the induced magnetic field strength can, based on their features, be classified as either magnetized or unmagentized (Luhmann et al., 1980; Luhmann & Cravens, 1991). When the solar wind pressure exceeds the peak ionospheric thermal pressure, the planet's induced field is classified as being in a magnetized state. In the magnetized state, the vertical profile contains a local minimum near 200 km and a local maximum near 170 km with peak field strengths up to 150 nT. Alternatively, when the solar wind pressure is less than the peak ionospheric thermal pressure, the ionosphere is in an unmagnetized state (Luhmann & Cravens, 1991). In the unmagnetized state, the ionosphere excludes most of the external field and the low-altitude induced field strength is weaker (< 30 nT). These profiles lack distinct maxima or minima at low altitudes, but instead contain many small-scale (∼10 km) spikes characterized as flux ropes (Elphic et al., 1980; Phillips et al., 1984a; Elphic & Russell, 1983).

Some basic characteristics of the low-altitude field strengths in the magnetized ionosphere of Venus have also been reported. The low-altitude field strength was found to decrease with increasing solar zenith angle (SZA) (Luhmann & Cravens, 1991). Additionally, the field strength was found to increase with increasing solar wind dynamic pressure (Luhmann et al., 1980; Kar & Mahajan, 1987). Both of these variations are expected if pressure balance is satisfied across the near-space environment and the induced field is required to balance the dynamic pressure of the oncoming solar wind (Luhmann & Cravens, 1991; Sánchez-Cano et al., 2020). Starting in the pristine solar wind and moving inward, the dominant pressure terms are as follows: the dynamic pressure in the solar wind, the plasma thermal pressure in the sheath, the magnetic pressure in the magnetic pileup region, and the sum of the plasma thermal pressure and induced magnetic pressure below the magnetic pileup boundary. Essentially, the perpendicular component of the solar wind dynamic pressure is ultimately converted into magnetic pressure in the magnetic pileup region.

Mars Global Surveyor (MGS) provided the first comprehensive magnetic field measurements at Mars, discovering the total field is a combination of induced fields and crustal fields that are scattered across the planet (Connerney et al., 2001; Brain, 2003). However, MGS was unable to measure the induced magnetic field at low altitudes. Arriving at Mars in 2014, the Mars Atmosphere and Volatile EvolutioN (MAVEN) mission became the first spacecraft to routinely measure low-altitude magnetic fields. Recently, Fang et al. (2023) analyzed low-altitude magnetic field data from MAVEN. They found the induced field strength on the dayside is usually around 15-50 nT, decreases with increasing SZA, and increases with increasing solar wind dynamic pressure. Huang et al. (2023) found the vertical profiles often resemble a reversed "L": above ∼200 km the field has a constant value, and below ∼200 km the field abruptly decreases in strength. Several studies have also examined the ubiquitous small scale features (10-50 km) present in the observed magnetic field profiles, including waves, slabs, flux ropes, and flux tubes (Hamil et al., 2022; Bowers et al., 2021; Cravens et al., 2023). These structures are thought to form through a variety of processes such as variations in the upstream solar wind, global plasma dynamics, and plasma instabilities.

Models have been used in attempt to reproduce the observed low-altitude magnetic field profiles at both planets. For Venus, models from the PVO era (Cloutier, 1984; Cravens et al., 1984; Luhmann et al., 1984; Shinagawa & Cravens, 1988; Luhmann & Cravens, 1991) and more recent iterations (Y. Ma et al., 2020, 2023), have been quite successful at reproducing the observed large-scale magnetic fields present in the magnetized ionosphere. They are able to reproduce several features of the magnetized profiles, including the local minimum near 200 km and the local maximum near 170 km (Cravens et al., 1984; Phillips et al., 1984b; Cloutier, 1984; Shinagawa & Cravens, 1988). Similar models for the induced field at Mars have been somewhat successful at reproducing the observed profiles (Shinagawa & Cravens, 1989; Y. J. Ma et al., 2017; Fang et al., 2018; Huang et al., 2023). Generally, however, the observed induced field profiles at Mars have more small-scale features that models are unable to fully reproduce.

In these models, the evolution of the induced magnetic field, B_{ind}, is described by the magnetic diffusion equation (Luhmann & Cravens, 1991):

$$\frac{\partial B_{ind}}{\partial t} = \nabla \times (u \times B_{ind}) - \nabla \times (\eta_m \nabla \times B_{ind}) \tag{1}$$

where t is time, u is the plasma flow speed, and η_m is the magnetic diffusivity. The first term in Equation 1 represents the convection of magnetic flux with plasma flow. The second term represents the diffusion or dissipation of the magnetic field as the electrical currents associated with the field are dampened through collisions (Luhmann & Cravens, 1991). At the top of the ionosphere, which is sometimes called the magnetic pileup bound-

ary or ionopause (Espley, 2018), densities are so low that the first term dominates and the draped solar wind field is convected into the ionosphere by downward flowing plasma. As the field is convected downward, the diffusion term eventually takes over as increased ion-neutral collisions between the induced current and neutral molecules causes the field to dissipate. The vertical structure of the induced magnetic field profile is, to first order, controlled by these processes. An interesting aspect of this picture is that variations in upstream solar wind conditions, such as a change in dynamic pressure, will not have an immediate affect in the low-altitude induced field because the effects take time to propagate through the sheath and into the ionosphere (Luhmann et al., 1984; Y. Ma et al., 2020; Hamil et al., 2022; Cravens et al., 2023).

In this work, our aim is to compare the structure and variability of the low-altitude induced magnetic fields at Venus and Mars. Our focus is on large scale structures as opposed to the small-scale structures like flux ropes. Our primary goals are to (1) investigate if the vertical structure of the induced magnetic field profiles at Mars can, like at Venus, be classified as magnetized or unmagnetized; (2) compare the induced field strengths at each planet and investigate if they are consistent with pressure balance, and (3) determine if the low-altitude induced magnetic field strengths vary with SZA and solar wind dynamic pressure in similar ways.

2 Data and Method

2.1 Pioneer Venus Orbiter

PVO collected the bulk of its low-altitude in situ measurements between December 1978 and July 1980 when its orbital period was 24 hours, and periapsis altitude was maintained near 160 km for nearly 700 orbits (Brace & Kliore, 1991). During this time, the periapsis segment evolved to cover a wide range of local times and solar zenith angles, but stayed near mid-latitudes throughout (10°S-40°N).

For magnetic field data, we use the low resolution magnetometer (OMAG) observations that have 12-second time resolution (C. T. Russell et al., 1980). The files contain the magnetic field vector, spacecraft altitude, solar zenith angle, and latitude of each observation. Each orbit is split into an inbound and outbound segment and the observations are trimmed to only include altitudes below 500 km. For upstream solar wind data, we use the upstream measurements from PVO that were obtained when PVO was located outside the bow shock. The IMF vector was measured by OMAG and the solar wind density and velocity were measured by the Plasma Analyzer instrument (Intriligator et al., 1980). The data are provided as hourly averages but we assign a single value to each half-orbit (inbound and outbound) by taking the solar wind measurement closest in time to the low-altitude magnetic field (periapsis) measurement. Periapsis segments without a solar wind measurement within 10 hours were not included. The dataset provides solar wind proton densities and velocities from which we calculate the dynamic pressure using $P_{sw} = \rho V^2$ where P_{sw} is the solar wind dynamic pressure, ρ is the solar wind mass density, and V is the bulk flow velocity.

2.2 MAVEN

The Mars low-altitude in situ measurements cover October 2014 through August 2020 when MAVEN' orbital period was 4.5 hours and periapsis altitude varied between ∼150-200 km. A handful of the observations come from times when periapsis was lowered down to ∼125 km for week-long "deep dip" campaigns (Jakosky et al., 2015). The location of MAVEN's periapsis segment slowly evolves throughout the mission, covering a wide range of latitudes, local times, and SZAs. For magnetic field data, we use the Key Parameter (KP) data products. The KP data are a bundle that includes measurements from every MAVEN in situ instrument along with spacecraft ephemeris informa-

tion, all on a uniformly sampled 4-second time grid. The KP files are compiled from the instrument's fully calibrated Level 2 data products. As with the Venus data, each orbit is split into an inbound and outbound segment and trimmed to only include observations at an altitude below 500 km.

For solar wind data, we use observations from MAVEN's Magnetometer (MAG) and Solar Wind Ion Analyzer (SWIA) that were obtained while MAVEN was outside the bowshock. The data are derived using the method described in (Halekas et al., 2017), which provides averages of solar wind properties for each orbit. The SWIA observations contain the solar wind proton density and velocity which are used to calculate the solar wind dynamic pressure. Periapsis segments without a solar wind measurement within 10 hours were not included. However, many of the orbits do not have upstream solar wind measurements within 10 hours of the periapsis observations. To fill these gaps, we use the Ruhunusiri et al. (2018) solar wind proxy model, which predicts upstream solar wind conditions based on MAVEN observations in the sheath. Of the 2625 MAVEN profiles in the final dataset, 1151 were assigned upstream conditions based on SWIA observations, 1069 were assigned from the proxy model, and 405 could not be assigned.

2.3 Caveats

When comparing results derived from the MAVEN and PVO observations, several differences between the two datasets must be considered. First, the PVO data were obtained during the maximum of Solar Cycle 21 (Brace & Kliore, 1991), while the MAVEN data were obtained during the declining phase of the rather weak Solar Cycle 24 (Lee et al., 2017). Second, the PVO periapsis is confined to mid-latitudes, while the MAVEN periapsis covers latitudes between 75° N and 75° S (see Figure 1). Additionally, because the spacecraft moves both vertically and horizontally during each periapsis pass, the structures we observe in the magnetic field profiles may not strictly be in the vertical direction.

Differences between the planets themselves must also be kept in mind when comparing results from the two planets. For example, Mars has rather pronounced seasons due to its eccentric orbit and 25° axial tilt, while Venus has no seasons because of its circular orbit and $< 3°$ axial tilt. Other differences to consider include, but are not limited to, planetary rotation rate, the presence of crustal magnetic fields at Mars but not Venus, planetary size, and planet-Sun distance.

2.4 Method

The vertical structure of the induced magnetic field profiles at Venus can generally be categorized into one of two states: "magnetized" or "unmagnetized". We categorize the Venus profiles in this manner based on the descriptions in Luhmann and Cravens (1991). If the global minimum of a trimmed magnetic field profile is below 300 km, and the profile has low-altitude (< 250 km) maximum field strength greater than 30 nT, it is classified as magnetized. If a profile has a low-altitude magnetic field strength greater than 50 nT, it is also classified as magnetized. Alternatively, If a profile has a low-altitude maximum field strength less than 30 nT, it is classified as unmagnetized. A small number of profiles remain categorized because they they do not match either criteria.

Figure 3 shows six examples of Venus magnetic field profiles observed by PVO. The examples in the left column show magnetized profiles. They contain a peak below 200 km, a wide minimum near 200-250 km, and a nearly-constant topside. These features are all absent in unmagnetized profiles, examples of which are shown in the right column of Figure 3. Instead, the unmagnetized profiles are nearly featureless, lacking distinct maxima or minima, and have weaker field strengths at nearly all altitudes.

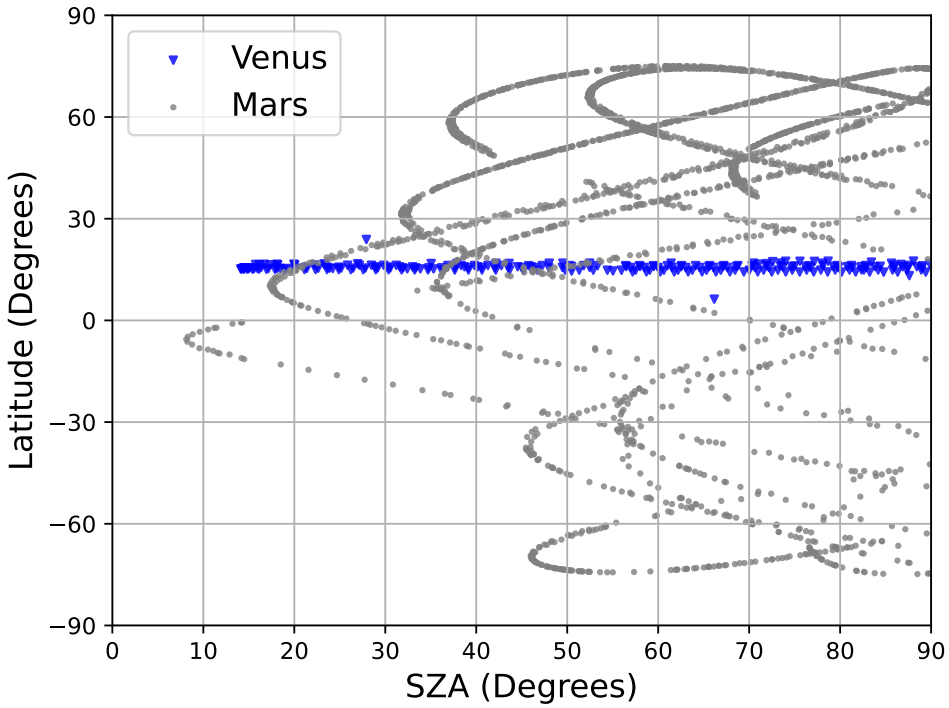

Figure 1: The latitudes and solar zenith angles at periapsis for the orbits used in this study, demonstrating the observational coverage of PVO (blue triangles) and MAVEN (gray circles) are quite different.

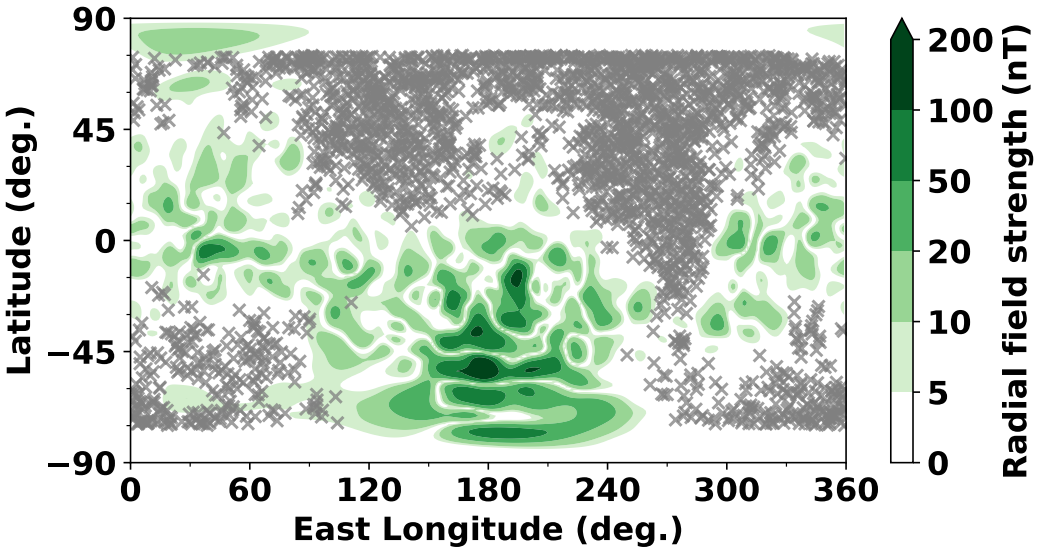

Figure 2: Locations of the MAVEN observations used in our analysis. Grey X's show locations of low-altitude maximum magnetic field strengths (B_{max}) for each inbound and outbound profile. Green contours are a map of the Martian radial crustal field strength at 400 km (Morschhauser et al., 2014). These locations are chosen because they are from weak crustal field regions, making them more comparable to Venus.

Figure 4 shows six examples of magnetic field profiles observed by MAVEN. These profiles are much more complicated than profiles from Venus and they lack recognizable features that would allow them to be sorted easily into two categories. This issue will be explored further in Section 3.1.

Since we are interested in comparing the strength and variability of the low-altitude induced fields at Venus and Mars, we focus our analysis on the maximum magnetic field strength below 250 km altitude (B_{max}). To derive B_{max} for both inbound and outbound segments of an orbit, we locate the maximum field strength below 250 km. This altitude cutoff of 250 km was chosen because it will capture the low-altitude peaks around 170 km in the magnetized profiles at Venus (Luhmann & Cravens, 1991), and be flexible enough to capture peaks in the Mars profiles at a wide range of altitudes. The B_{max} derived from each Venus profile is marked in Figure 3. For magnetized profiles, B_{max} is the field strength at the location of the low-altitude peak near 170 km. For unmagnetized profiles, B_{max} is the maximum field strength below 250 km, but is not at the location of any specific feature. The same method is used to extract B_{max} from the Mars profiles, which are marked in Figure 4. Since the vertical structure varies much more from profile to profile, the derived B_{max} is not extracted from a recurring distinct feature, as in the case of the magnetized Venus profiles.

We note that there are several cases when the location of the derived B_{max} is either at the bottom of the profile (periapsis) or at the top of the profile (near the top altitude cutoff of 250 km). For cases when the derived B_{max} is near the top of the profile, the low-altitude field strength never exceeds the field strength at 250 km. Examples of this case can be seen in Figures 3E and 4B. For these, B_{max} is likely overestimated because our method does not pick any low-altitude feature that has a local maximum below 250 km. For cases when B_{max} is near periapsis, the derived B_{max} likely underestimates the true local maximum in the low-altitude magnetic field profile because the true maximum may reside below periapsis where there are no observations. Examples of this case can be seen in Figure 3C and 4D. With these caveats in mind, we include these cases in our final dataset.

Another important consideration is the crustal magnetic fields at Mars that are not at Venus. We wish to remove these crustal fields from our analysis to enable a more direct comparison between the two planets, focusing solely on the induced component of the magnetic field. The Morschhauser et al. (2014) empirical model of crustal magnetic field strength is used to omit MAVEN observations where the crustal field strength is comparable to the induced field strength. More concretely, we exclude any profiles that have $B_{crust}/B_{max} > 0.2$ where B_{crust} is the crustal field strength at the location of B_{max}. Figure 2 shows the locations of B_{max} that remain after applying this crustal field filtering. It demonstrates the chosen B_{max}'s are confined to outside the crustal field regions.

To focus on the dayside interaction region, in our final dataset we only use profiles that have B_{max} at SZA $< 90°$. In total, the final filtered dataset for Venus includes 475 magnetic field profiles of which 188 are categorized as magnetized, 260 as unmagentized, and 27 as uncategorized. Of the 188 magnetized profiles, 39 have B_{max} at the bottom of the profile and 25 have B_{max} at the top altitude cutoff of 250 km. Of the 260 unmagentized profiles, 6 have B_{max} at the bottom of the profile and 30 have B_{max} at 250 km. The final filtered dataset for Mars includes 2625 profiles. Of these, 220 have B_{max} at the bottom of the profile and 112 have B_{max} at the top altitude cutoff of 250 km.

3 Analysis

3.1 Categorizing the Magnetic Field Profiles

As discussed in Section 2.4 and shown in Figure 3, the induced magnetic field profiles at Venus have reccurring vertical structures that can generally be categorized as ei-

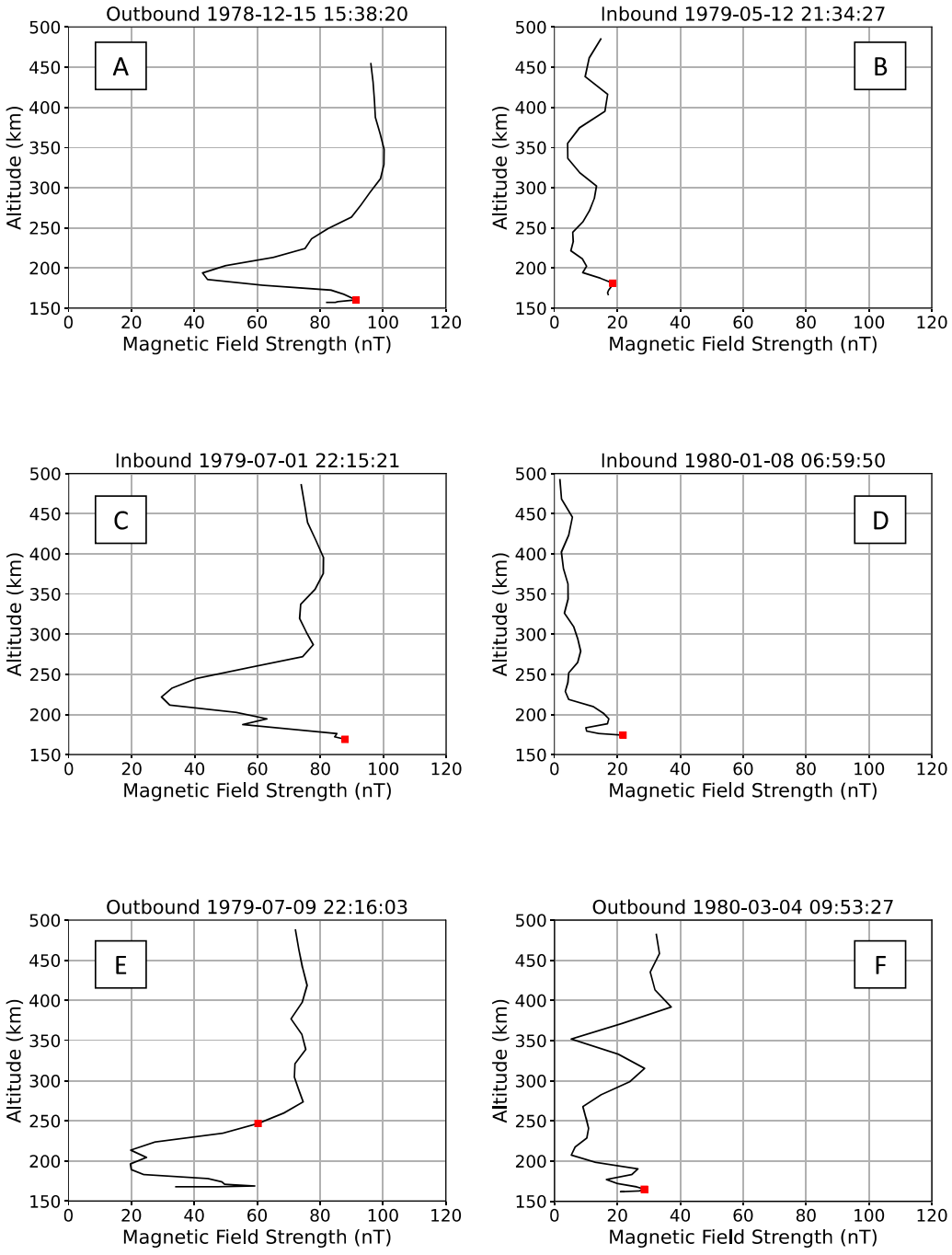

Figure 3: Examples of magnetic field profiles from Venus with magnetized states in the left column and unmagnetized states in the right column. The squares mark the derived B_{max} for each profile.

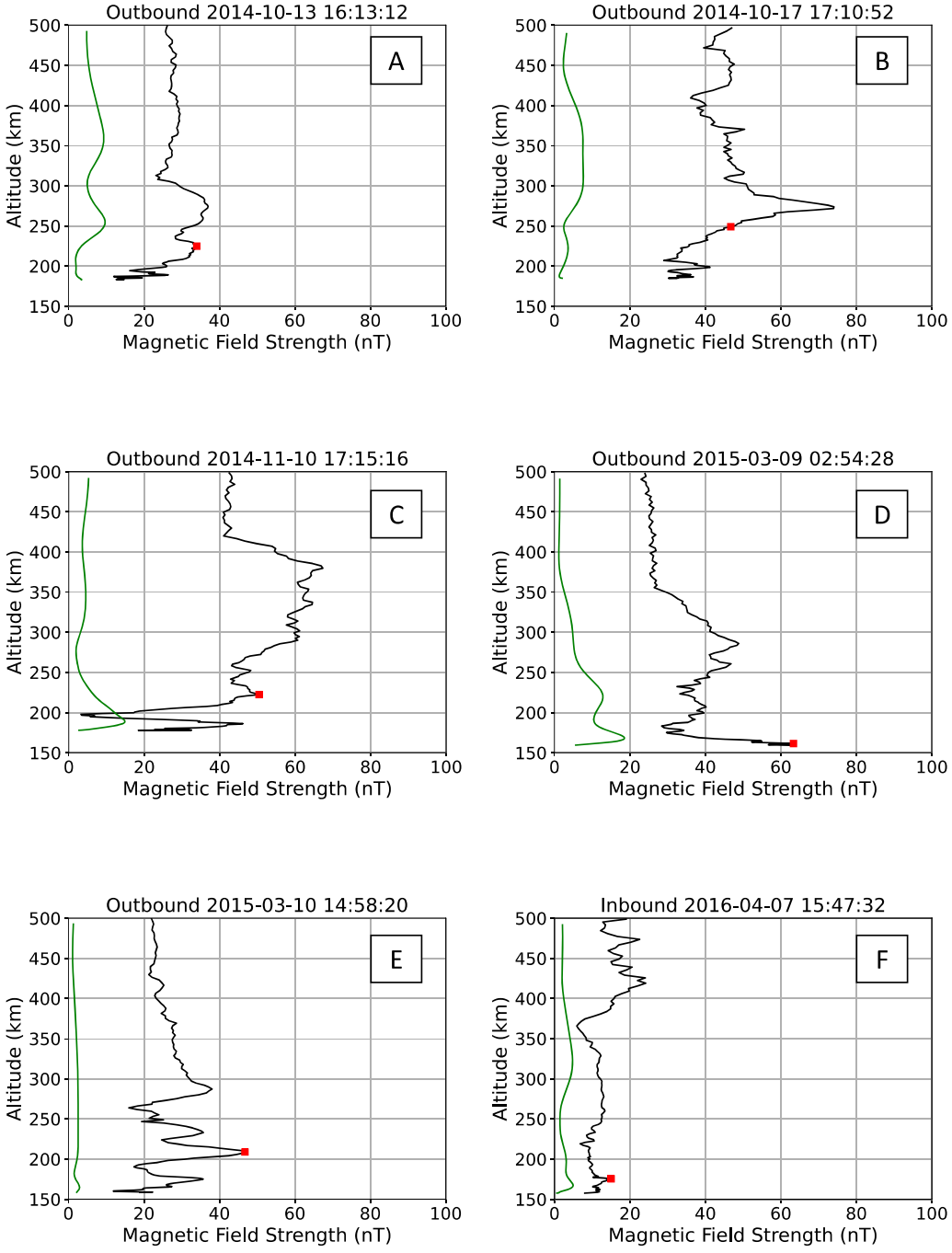

Figure 4: Examples of magnetic field profiles from Mars. The black lines are the measured magnetic field from MAVEN and the green lines are the crustal magnetic field strength from the Morschhauser et al. (2014) crustal field model. The red squares mark the derived B_{max} for each profile.

ther "magnetized" or "unmagnetize" (Luhmann & Cravens, 1991). Using our classification criteria, we find ∼40% of the profiles can be classified as magnetized and ∼55% can be classified as unmagnetized. These percentages are loosely consistent with the occurrence rates reported by Luhmann et al. (1980), who categorized 30% as magnetized and 70% as unmagnetized. However, they used somewhat different classification criteria.

We attempted to categorize the Mars profiles based on visual inspection but quickly found they could not be categorized into Venus-like magnetized and unmagentized vertical structures. This is demonstrated in Figure 4, which shows the Mars profiles lack distinct features that would enable them to be easily categorized. In particular, they lack a consistent minimum near 300 km or a clear single low-altitude peak, features that are present in the Venus magnetized profiles. Instead, the Mars profiles are more varied and have more complex small-scale structures (tens of kilometers). These structures are present even when the crustal field component is much lower than induced field strength.

We conclude the vertical structure of the induced magnetic fields at Mars are too varied to be classified into simple magnetized and unmagnetized states. Further, it is generally accepted that Mars is magnetized more often than Venus, meaning the ionospheric thermal pressure is usually insufficient to exclude the external field from penetrating into the ionosphere (Zhang & Luhmann, 1992; Chu et al., 2021; Holmberg et al., 2019; Sánchez-Cano et al., 2020). Profiles resembling the magnetized ionosphere of Venus, such as the profile shown in Figure 4C, do exist but are quite rare.

Although the induced magnetic field profiles at Mars are unable to be categorized into simple states like at Venus, there are some reoccurring features that are worth reporting. First, the profiles often have a distinct prominent peak between 250-300 km. Examples of such profiles can be seen in Figure 4A, B, and D. Some profiles have many peaks, such as the one shown in Figure 4E. These multiple peaks at low altitudes may be due to a combination of both horizontal and vertical variations in the magnetic field strength (the spacecraft trajectory is not strictly vertical). Generally, magnetized profiles at Venus lack such a complicated structure.

Neither the complicated multi-peaked structures, nor a peak between 250-300 km were predicted by the earliest MHD models (Shinagawa & Cravens, 1989). More recent MHD studies that include the time-dependent effects of changing solar wind conditions do predict more complicated structures including a peak between 250-350 km (Y. J. Ma et al., 2014, 2017). The peaks are caused by vertical gradients in the downward plasma flow speed as a result of solar wind pressure variations on hour long timescales. Solar wind variations may be responsible for some of these small scale features (Cravens et al., 2023), but other processes such as plasma instabilities and global plasma dynamics likely play a role (Hamil et al., 2022).

3.2 Solar Zenith Angle Variations

To first order, we expect pressure balance to be maintained through the space environment. Given this assumption, the maximum induced magnetic field strength should depend on the solar wind dynamic pressure and the ionospheric thermal pressure. To achieve pressure balance, higher solar wind dynamic pressures should lead to stronger induced fields, while higher ionospheric thermal pressures should be able to exclude the solar wind field more efficiently, resulting in weaker induced fields. Mathematically, if pressure balance is satisfied throughout the low-altitude ionosphere then

$$P_{sw} cos^2(\chi) = P_{th} + P_B \tag{2}$$

where $P_{sw}cos^2\chi$ is the normal component of the solar wind dynamic pressure (Crider et al., 2003), χ is SZA, P_{th} is the ionospheric thermal pressure, and $P_B = B_{ind}^2/2\mu_o$ is the induced magnetic field pressure. If we also assume $P_B >> P_{th}$, which is often the case at Mars (Holmberg et al., 2019; Sánchez-Cano et al., 2020), then we expect the induced field strength to approximately follow

$$B_{ind} = (2\mu_o P_{sw})^{1/2} cos(\chi) \tag{3}$$

where μ_o is the vacuum permeability. This equation predicts that, when magnetized ($P_B > P_{th}$), the induced magnetic field strength should be approximately proportional to cosine of the SZA. We examine this prediction for both Venus and Mars.

Figure 5 shows B_{max} plotted against SZA for both planets. The Venus observations are separated into their magnetized and unmagnetized classifications, but not separated based on solar wind dynamic pressure because of data scarcity. The Mars observations are sorted into groups based on solar wind dynamic pressure since the induced field will increase with increasing solar wind pressure (see Section 3.4). The data are binned along the SZA axis using uneven bin sizes so that each bin has a comparable number of data points.

At Venus the maximum field strengths of the unmagnetized profiles do not have a SZA dependence and are around 20 nT, which is consistent with previous studies (Elphic et al., 1984). The low field strengths are expected because, when unmagnetized, the external magnetic field is excluded from the ionosphere by the high ionospheric thermal pressure, and thus the induced field strength is not expected to be driven by the solar wind pressure. In these cases $P_B << P_{th}$ so Eq. 3 is not applicable and we do not expect any cosine dependence. In contrast, the maximum field strengths of the magnetized profiles decrease with increasing SZA up to a SZA of $\sim$65°. The bin-averaged maximum field strength decreases from $\sim$80 nT near the subsolar point to $\sim$40 nT near 65° SZA. This is consistent with previous work which has shown that this SZA trend is approximately satisfied in the magnetized Venus ionosphere, but the analysis was conducted with few observational data points (C. Russell et al., 1983).

Similarly, the maximum field strengths at Mars decrease from $\sim$70 nT (35 nT) at the subsolar point to $\sim$40 nT (25 nT) around 75° SZA during high (low) solar wind dynamic pressure. There is also clear separation between the dynamic pressure bins, with higher maximum field strengths occurring during higher solar wind dynamic pressures, as predicted by Equation 3. The solar wind dynamic pressure trends at both planets will be further explored in Section 3.4.

The dotted lines shown in Figure 5 are fits to the data using SZA for χ in Equation 3. Specifically, we fit the binned averages to $B_{max} = B_0 cos(\chi)$ where B_0 is a fit parameter that represents the subsolar induced field strength. In both cases, the data are poorly fit. We suggest this deviation from the prediction is a consequence of SZA being only an approximation of the angle between the solar wind bulk flow velocity and the obstacle. We refit the data after replacing χ with θ, where θ is the angle between the solar wind flow and the MPB (Crider et al., 2003). For Venus we use the MPB shape found by Xu et al. (2021) and for Mars we use the MPB shape given in Vignes et al. (2000). The fits are markedly improved when using θ in place of SZA. It is especially apparent at Mars that the trend follows the shape of the MPB rather than of cosine of SZA. The fit parameter (B_0) for Venus is 79.5±0.9. The fit parameters for Mars are 79.2±0.4, 51.7±2.0, and 40.1±1.4 for the high, medium, and low solar cases , respectively.

From these two plots we conclude low-altitude maximum field strength follows the predicted cosine trend (Eq. 3) up to at least 60° when in a magnetized state, but only if the angle between the solar wind flow and the MPB is used (θ). However, near the ter-

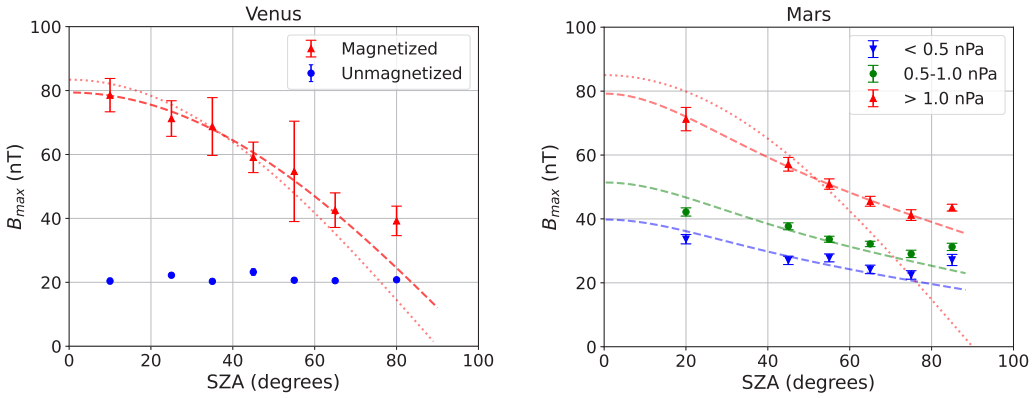

Figure 5: The solar zenith angle (SZA) variation of B_{max} for Venus (left) and Mars (right). The dotted lines are fits to $B_{max} = B_0 cos(\chi)$ (see Equation 3) using SZA for χ. The dashed lines are fits using θ (the angle between the solar wind flow and the magnetic pileup boundary) in place of χ (Vignes et al., 2000; Xu et al., 2021). The Venus data are sorted into magnetized and unmagnetized cases while the Mars data are sorted into solar wind dynamic pressure bins. Error bars show the standard error in each bin. The solar zenith angle bins for Venus have edges at 0°, 20°, 30°, 40°, 50°, 60°, 70°, and 90°. The SZA bins for Mars have edges at 0°, 40°, 50°, 60°, 70°, 80°, and 90°.

minator B_{max} is higher than predicted at both planets. We currently do not have an explanation for this observed deviation.

3.3 Peak Magnetic Field Distributions

In Figure 6A, we plot histograms of B_{max} with the Venus data separated into magnetized and unmagnetized categories (Section 3.1). All the B_{max} values from Mars and all the magnetized B_{max} values from Venus are corrected to the subsolar point by dividing them by $cos(\theta)$. Only B_{max} values at SZA $< 60°$ are included (Section 3.2). The histogram of the unmagnetized B_{max} values at Venus form a sharp peak around 20 nT, which is the typical magnitude of the induced field when unmagnetized. The histogram of the magnetized B_{max} values at Venus form a much wider distribution, but demonstrates the clear demarcation between magnetized and unmagentized states. The magnetized distribution has a mean of 77.8 ($\pm$29.2) nT and a median of 75.7 nT. Comparatively, the distribution of the Mars B_{max} values has a mean of 62.9 ($\pm$29.4) nT and a median of 55.7 nT.

At the subsolar point, Equation 3 predicts $B_{max} = (2\mu_o P_{sw})^{1/2}$ (Fang et al., 2023). Since P_{sw} scales as the inverse square of the planet-Sun distance, we expect larger B_{max} values at Venus than Mars, which is confirmed in Figure 6. Given the inverse square law, Equation 3 predicts $\frac{B_{max,\text{Venus}}}{B_{max,\text{Mars}}} \simeq \frac{1.5\text{AU}}{0.7\text{AU}} \simeq 2.1$. However, the observed ratio is only 1.2 if using the means of the distributions (77.8 nT/62.9 nT), or 1.4 if using the medians (75.7 nT/55.7 nT). If we account for the crustal field component at Mars, that is at most 20% of B_{max} (in most cases is less than 10% of B_{max}), then the observed ratio is at most 1.75 (1.4/0.8), still implying the observed ratio is smaller than the prediction of 2.2.

To explore why the ratio is smaller than predicted, Figure 6B shows a comparison of the observed and predicted B_{max}. In particular, the histograms show the ratio between the observed B_{max} and the predicted B_{max} for each profile. Only observations with SZA $< 60°$ are included. The Venus ratios are usually less than one, having a mean of 0.66

(±0.22) nT. A possible explanation is that Equation 3 relies on two assumptions: (1) pressure balance throughout the space environment and (2) the ionospheric thermal pressure is negligible compared to the magnetic pressure. At Venus, the second assumption is often not satisfied (Luhmann et al., 1987) leading to a reduction in the induced field strength via Equation 2.

At Mars, the ratios are usually greater than one, with a mean of 1.38 (±0.22) nT. If we consider a 20% crustal field component, the mean would decrease to at least 1.1, still implying the induced field strengths at Mars are somewhat larger than predicted by Equation 3. Since the second assumption is usually satisfied at Mars (Holmberg et al., 2019; Chu et al., 2021; Sánchez-Cano et al., 2020), it might be expected that Equation 3 is a good predictor of the maximum induced field strength. A possible explanation for why B_{max} is usually larger than the prediction is the presence of small-scale features in the magnetic field profile. These small scale features are much more prevalent at Mars than at Venus. They result in small-scale spikes and bumps that can lead to a higher B_{max} than predicted. These small scale structures arise from a variety of processes, such as waves, rotations, plasma instabilities (Hamil et al., 2022; Cravens et al., 2023).

Lastly, Figure 6c shows histograms of the altitude where B_{max} is observed. At Venus, the altitude of the low-altitude maximum induced field, when magnetized, is consistently around 170 km. There are rarer cases where the altitude of B_{max} is much higher, including a number of profiles with the altitude bin in the highest histogram bin near 250 km. These are the edge cases discussed in Section 3.3 and are profiles similar to Figure 3E. The peak altitude at Mars is typically between 160-200 km, but the distribution is much wider than the distribution at Venus. The distribution is likely wider because of seasonal variations in the upper atmosphere of Mars, which causes constant pressure levels to rise and fall over the year owing to the changing insolation from Mars' elliptical orbit.

3.4 Solar Wind Dynamic Pressure

It is expected that with increasing solar wind pressure, the induced field strength will increase. Assuming pressure balance across the magnetic pileup boundary and into the ionosphere, and negligible ionospheric thermal pressure, the induced field strength should vary as the square root of the solar wind dynamic pressure (Eq. 3). Previous work has shown that the magnetic field at the MPB does respond in this manner to solar wind dynamic pressure variations (Crider et al., 2003; Xu et al., 2021). Below the MPB, we still expect the induced field to increase with increasing dynamic pressure because the fields at the MPB are convected downward into the ionosphere.

Figure 7 shows the dependence B_{max} on solar wind dynamic pressure. The magnetized Venus data, and the Mars data, are corrected to the subsolar point by dividing them by $cos(\theta)$ (see Section 3.2). The plot only contains data with SZA $< 60°$. We fit a power law to the observations: $B_{max} = B_0 P_{sw}^n$ where B_0 is the best-fit subsolar B_{max} and n is the best-fit exponent. B_{max} increases with solar wind pressure for both Venus (when magnetized) and Mars with power law exponents $n = 0.57 \pm 0.13$ and $n = 0.45 \pm 0.02$ respectively. These are consistent with each other within error, however the Venus fit has significant uncertainty due to having much fewer data points and a more narrow range of solar wind pressure coverage compared to Mars. The R-squared value of the fits is 0.2 for Venus (magnetized) and 0.6 for Mars.

The coefficient B_0 of the power law fit for Venus (magnetized) is 27.7±6.1 whereas the coefficient for Mars is 65.2±0.7. This implies that for a solar wind pressure of 1 nPa, Mars would have a higher induced field, which is expected since Venus tends to exclude the external magnetic field more effectively than Mars (consistent with figure 6c). However, Venus is more likely to experience higher solar wind dynamic pressure since it is closer to the Sun. As a result, the average B_{max} for Venus (when magnetized) is higher than at Mars (see Section 3.3).

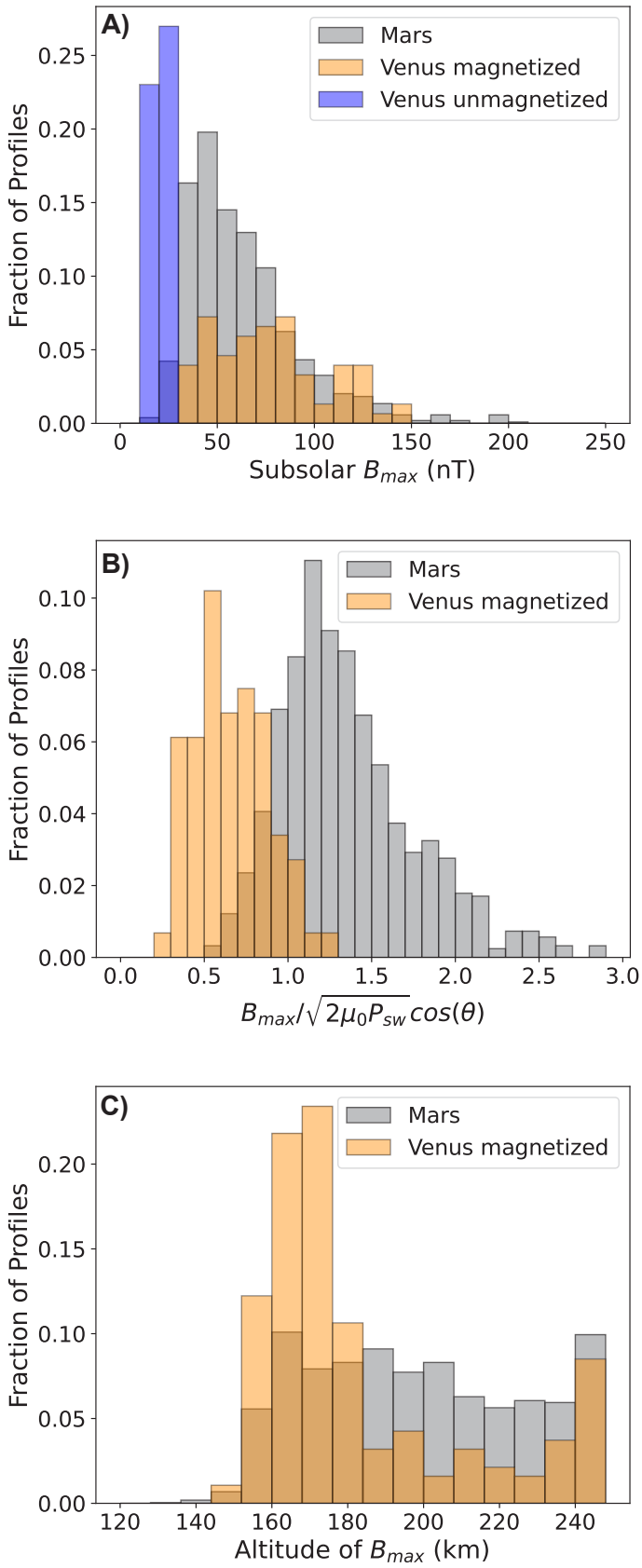

Figure 6: (A) Histograms of B_{max}, the maximum low-altitude field strength. (B) Ratios of the observed B_{max} and the B_{max} predicted by Equation 3. (C) Histograms of the altitude of B_{max}.

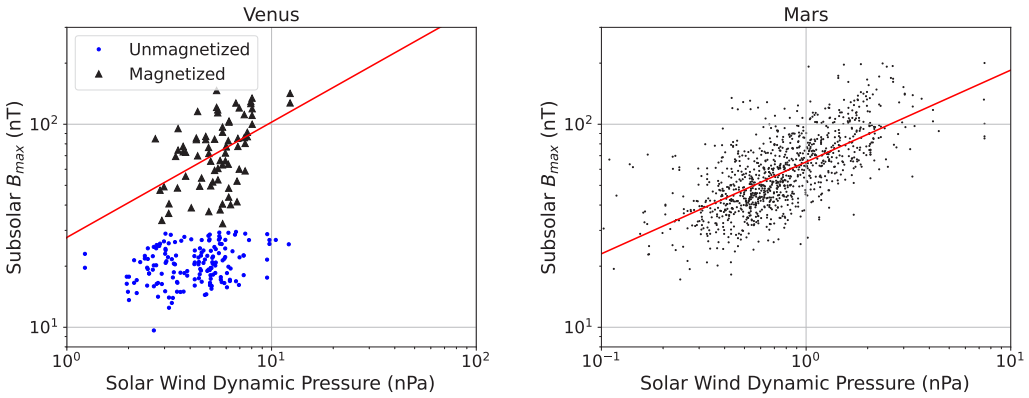

Figure 7: The variation of B_{max} with solar wind dynamic pressure for Venus (left) and Mars (right). For Venus, values derived from magnetized profiles are plotted as black triangles and values derived from unmagnetized profiles are plotted as blue circles. The red lines are power law fits with derived exponents of 0.57±0.13 for Venus (magnetized) and 0.45±0.02 for Mars.

The induced field strength of the unmagentized ionosphere of Venus has virtually no dependence on solar wind dynamic pressure. The best-fit exponent is zero and the R-squared value is 0.01. This lack of dependence on solar wind pressure is expected because, when unmagnetized, the solar wind magnetic field is excluded from low altitudes by the ionospheric thermal pressure.

4 Discussion and Conclusions

In this study, we compare low-altitude induced magnetic fields at Venus and Mars. Our main results are as follows:

1. The magnetic field profiles at Venus and Mars have different altitude structures. The magnetized profiles at Venus have distinct, identifiable features, namely a peak in magnetic field around 170 km, a wide minimum around 200 km, and a nearly constant topside above 250 km. But the Mars profiles lack these distinct, repeatable large-scale features that would allow them to be classified into magnetized and unmagnetized categories like Venus.
2. The maximum low-altitude magnetic field strength (B_{max}) in the unmagnetized ionosphere of Venus has no dependence on SZA. The B_{max} in the magnetized ionosphere of Venus, and the B_{max} at Mars, have a SZA dependence where $B_{max} \propto \cos(\theta)$ where θ is the angle between the solar wind velocity and the MPB normal vector (Eq. 3). However, at both planets, B_{max} is larger near the terminator than this trend predicts.
3. The mean Venus B_{max} (77.8 nT) is greater than the mean Mars B_{max} (62.9 nT) which is expected since Venus is exposed to higher solar wind pressures. When comparing B_{max} with the prediction from Eq. 3 — which is derived assuming pressure balance is maintained and $P_{th} << P_B$ — the B_{max} at Venus (magnetized) is lower than predicted by a factor of 0.66. The B_{max} at Mars, alternatively, is higher than predicted by a factor between 1.1 and 1.38.
4. When unmagnetized, Venus B_{max} has no dependence on solar wind dynamic pressure (P_{sw}). When magnetized, Venus B_{max} has a dependence of $B_{max} \propto (P_{sw})^{057\pm.13}$, which is potentially consistent with the prediction from Equation 3 of an expo-

nent of 0.5. However, the fit is poor and the dynamic pressure can only account for 20% of the variation in B_{max}. The Mars B_{max}, in contrast, has a dependence of $B_{max} \propto (P_{sw})^{0.45\pm.02}$, and the dynamic pressure can account for 60% of the variation in B_{max}.

The vertical structure of the magnetic field profiles at Mars is highly varied and inconsistent, in contrast with the Venus profiles which tend to have the same recurring large-scale features. A likely explanation is the ubiquitous presence of small-scale structures in the magnetic field profiles at Mars, which are much less common in the magnetized ionosphere of Venus. This explanation was also put forth by Huang et al. (2023) to explain the varied magnetic field profiles at Mars. They attributed the varied structures to time-dependent variations in the up stream solar wind, such as variations in the solar wind dynamic pressure. The vertical structure of the Venus magnetic field profiles can be successfully reproduced by models, even under steady solar wind conditions (Luhmann et al., 1984; Cravens et al., 1984; Shinagawa & Cravens, 1988; Luhmann & Cravens, 1991). However, models have been less successful at reproducing the vertical structure of the Mars profiles. Additional physical processes likely need to be included to capture the small-scale structures (Hamil et al., 2022; Cravens et al., 2023).

We find both similarities and differences between the low-altitude magnetic field strengths. The main similarity arises between Mars and the magnetized ionosphere of Venus, providing further evidence that the ionosphere of Mars is magnetized most of the time (Sánchez-Cano et al., 2020). In particular, the low-altitude field strengths have the same SZA dependence, including higher than expected fields near the terminator. Further, at both planets the SZA variation of the low-altitude field strengths are modeled best when the angle between solar wind velocity and the normal vector of the MPB is used in Equation 3 (as opposed to SZA). In other words, since the low-altitude magnetic fields are convected downward from the MPB (Equation 1), the shape of the MPB controls how the strength of the low-altitude induced fields vary across the dayside ionosphere.

Major differences include higher induced field strengths in the magnetized ionosphere of Venus (means of 77.8 nT vs. 62.9 nT), which is expected given Venus is exposed to higher solar wind dynamic pressures due to its proximity to the Sun. Additionally, when magnetized, the low-altitude field at Venus is weaker than predicted under the assumptions of pressure balance and $P_{th} << P_B$ (Eq. 3). This is consistent with the fact that the assumption of $P_{th} << P_B$ is often unsatisfied at Venus because the ionospheric thermal pressure is often comparable to or greater than the solar wind dynamic pressure, especially during the PVO observations at solar maximum (Luhmann, 1986; Zhang & Luhmann, 1992). Consequently, the induced magnetic pressure does not have to be as large as the solar wind pressure to achieve pressure balance (Eq. 2).

In contrast, on Mars, low-altitude field strengths are higher than predicted by Equation 3, even after accounting for possible contributions from crustal fields. One possible explanation is again related to small scale features that are common at Mars but not at Venus. These observed small scale features may be either spatial (Hamil et al., 2022) or temporal (Huang et al., 2020) variations, and are likely driven by processes such as varying solar wind conditions, large-scale plasma dynamics, plasma instabilities, or current sheets (Hamil et al., 2022). The small scale features, such as the localized layers seen in Figure 4E, can increase the maximum low-altitude field strength so that is larger than predicted by Equation 3.

The increased presence of small-scale structures at Mars may be related to the convection and diffusion timescales, which characterize the time for the low-altitude induced fields to form and dissipate (Eq. 1). Recent calculations suggest the convection and diffusion timescales are on the order of a few hours at Venus (Y. Ma et al., 2020), but only on the order of tens of minutes at Mars (Huang et al., 2020). Given the timescales at

Mars can be shorter than the time it takes for MAVEN complete a low-altitude periapsis pass (∼10 minutes), it is possible some of the observed small-scale features are caused by temporal variations in the upstream solar wind, as suggested by Huang et al. (2020). However, these calculations are somewhat uncertain because they are strongly controlled by vertical plasma velocities, which are small (tens of m/s) and have not been directly measured (Y. Ma et al., 2020).

Taken together, our results reveal some interesting similarities and differences between the induced magnetic fields at Venus and Mars. They point to how planetary properties, such as planet-Sun distance, can affect the structure and variability of induced fields at unmagnetized planets. Being closer to the Sun, Venus has a higher ionospheric thermal pressure that is often comparable to or greater than the solar wind dynamic pressure (at least at solar maximum during the PVO observations). Consequently, it exhibits a dichotomy of magnetized and unmagnetized states, and in each state the induced field strength has a different dependence on SZA and solar wind dynamic pressure. Mars, being further from the Sun, has a lower ionospheric thermal pressure (from reduced solar EUV flux) and so the ionosphere is magnetized most of the time and does not exhibit a dichotomy of states. Further, the shape of the MPB controls the SZA variation of the induced fields at both planets, when in a magnetized state. This work focuses exclusively on weak crustal field regions at Mars, and future work focusing on strong crustal fields regions may reveal even more interesting differences between the low-altitude induced magentic fields at Venus and Mars.

5 Open Research

The data used in this work are publicly archived. The Venus magnetometer data can be found at `https://pds-ppi.igpp.ucla.edu/search/view/?f=yes\&id=pds://PPI/PVO-V-OMAG-4--SCCOORDS-24SEC-V2.0` and the Venus upstream solar wind data can be found at `https://cdaweb.gsfc.nasa.gov/cgi-bin/eval1.cgi`. The Mars Key Parameters data can be found at `https://lasp.colorado.edu/maven/sdc/public/data/sci/kp/` and the Mars upstream solar wind data can be found at `https://homepage.physics.uiowa.edu/~jhalekas/drivers.html`. The derived maximum low-altitude magnetic field strengths are publicly archived at `https://zenodo.org/uploads/10278080` for both Venus and Mars.

Acknowledgments

This work was supported by NASA grant 80NSSC21K0147 which was funded through the Solar System Workings program. S. Byrd received additional support from the NASA Iowa Space Grant Consortium and the John and Elsie Mae Ferentz Undergraduate Research Fund.

References

Bertucci, C., Duru, F., Edberg, N., Fraenz, M., Martinecz, C., Szego, K., & Vaisberg, O. (2011). The induced magnetospheres of Mars, Venus, and Titan. *Space Sci. Rev.*, *162*, 113–171.

Bowers, C. F., Slavin, J. A., DiBraccio, G. A., Poh, G., Hara, T., Xu, S., & Brain, D. A. (2021). MAVEN Survey of Magnetic Flux Rope Properties in the Martian Ionosphere: Comparison With Three Types of Formation Mechanisms. *Geophys. Res. Lett.*, *48*(10), e2021GL093296. doi: https://doi.org/10.1029/2021GL093296

Brace, L. H., & Kliore, A. J. (1991). The structure of the Venus ionosphere. *Space Sci. Rev.*, *55*, 81–163. doi: 10.1007/BF00177136

Brain, D. A. (2003). Martian magnetic morphology: Contributions from the solar

wind and crust. *Journal of Geophysical Research*, *108*(A12), 1424. doi: 10.1029/2002JA009482

Chu, F., Girazian, Z., Duru, F., Ramstad, R., Halekas, J., Gurnett, D. A., ... Kopf, A. J. (2021). The dayside ionopause of Mars: Solar wind interaction, pressure balance, and comparisons with Venus. *Journal of Geophysical Research: Planets*, *126*(11), e2021JE006936. doi: https://doi.org/10.1029/2021JE006936

Cloutier, P. A. (1984). Formation and dynamics of large-scale magnetic structures in the ionosphere of Venus. *Journal of Geophysical Research: Space Physics*, *89*(A4), 2401-2405.

Connerney, J. E. P., Acuña, M. H., Wasilewski, P. J., Kletetschka, G., Ness, N. F., Rème, H., ... Mitchell, D. L. (2001). The global magnetic field of Mars and implications for crustal evolution. *Geophysical Research Letters*, *28*(21), 4015–4018. doi: 10.1029/2001GL013619

Cravens, T. E., Hamil, O., Renzaglia, A., Ledvina, S. A., & Howard, S. K. (2023). Fourier analysis of magnetic fields in the ionosphere of Mars. *Journal of Geophysical Research: Space Physics*, *128*(4), e2022JA031044.

Cravens, T. E., Shinagawa, H., & Nagy, A. F. (1984). The evolution of large-scale magnetic fields in the ionosphere of Venus. *Geophysical Research Letters*, *11*(3), 267–270. doi: 10.1029/GL011i003p00267

Crider, D. H., Vignes, D., Krymskii, A. M., Breus, T. K., Ness, N. F., Mitchell, D. L., ... Acuña, M. H. (2003). A proxy for determining solar wind dynamic pressure at Mars using Mars Global Surveyor data. *J. Geophys. Res.*, *108*, 1461, 10.1029/2003JA009875. doi: 10.1029/2003JA009875

Daniell Jr, R., & Cloutier, P. (1977). Distribution of ionospheric currents induced by the solar wind interaction with Venus. *Planetary and Space Science*, *25*(7), 621–628.

Elphic, R. C., Brace, L. H., Theis, R. F., & Russell, C. T. (1984). Venus dayside ionospheric conditions - Effects of ionospheric magnetic field and solar EUV flux. *Geophys. Res. Lett.*, *11*, 124–127. doi: 10.1029/GL011i002p00124

Elphic, R. C., & Russell, C. T. (1983). Magnetic flux ropes in the Venus ionosphere: Observations and models. *Journal of Geophysical Research: Space Physics*, *88*(A1), 58-72. doi: 10.1029/JA088iA01p00058

Elphic, R. C., Russell, C. T., Slavin, J. A., & Brace, L. H. (1980). Observations of the dayside ionopause and ionosphere of Venus. *Journal of Geophysical Research*, *85*(A13), 7679. doi: 10.1029/JA085iA13p07679

Espley, J. R. (2018). The martian magnetosphere: Areas of unsettled terminology. *Journal of Geophysical Research: Space Physics*, *123*(6), 4521-4525. doi: 10.1029/2018JA025278

Fang, X., Ma, Y., Luhmann, J., Dong, Y., Brain, D., Hurley, D., ... Jakosky, B. (2018). The Morphology of the Solar Wind Magnetic Field Draping on the Dayside of Mars and Its Variability. *Geophysical Research Letters*, *45*(8), 3356–3365. doi: https://doi.org/10.1002/2018GL077230

Fang, X., Ma, Y., Luhmann, J., Dong, Y., Halekas, J., & Curry, S. (2023). Mars global distribution of the external magnetic field and its variability: Maven observation and MHD prediction. *Journal of Geophysical Research: Space Physics*, *128*(9), e2023JA031588. doi: 10.1029/2023JA031588

Halekas, J. S., Ruhunusiri, S., Harada, Y., Collinson, G., Mitchell, D. L., Mazelle, C., ... Jakosky, B. M. (2017, January). Structure, dynamics, and seasonal variability of the Mars-solar wind interaction: MAVEN Solar Wind Ion Analyzer in-flight performance and science results. *Journal of Geophysical Research: Space Physics*, *122*(1), 547–578. doi: 10.1002/2016JA023167

Hamil, O., Cravens, T. E., Renzaglia, A., & Andersson, L. (2022). Small scale magnetic structure in the induced martian ionosphere and lower magnetic pile-up region. *Journal of Geophysical Research: Space Physics*, *127*(4), e2021JA030139. doi: https://doi.org/10.1029/2021JA030139

Holmberg, M. K. G., André, N., Garnier, P., Modolo, R., Andersson, L., Halekas, J., ... Mitchell, D. L. (2019). MAVEN and MEX Multi-instrument Study of the Dayside of the Martian Induced Magnetospheric Structure Revealed by Pressure Analyses. *Journal of Geophysical Research: Space Physics*, *124*(11), 8564–8589. doi: 10.1029/2019JA026954

Huang, J.-P., Cui, J., Hao, Y.-Q., Guo, J.-P., Wu, X.-S., Niu, D.-D., & Wei, Y. (2020). Solar and Magnetic Control of Minor Ion Peaks in the Dayside Martian Ionosphere. *Journal of Geophysical Research: Space Physics*, *125*(8), e2020JA028254. doi: https://doi.org/10.1029/2020JA028254

Huang, J.-P., Hao, Y.-Q., Lu, H.-Y., & Cui, J. (2023). Variability of draped interplanetary magnetic field in the subsolar martian ionosphere. *The Astrophysical Journal*, *955*(1), 48.

Intriligator, D. S., Wolfe, J. H., & Mihalov, J. D. (1980, January). The Pioneer Venus Orbiter Plasma Analyzer Experiment. *IEEE Transactions on Geoscience and Remote Sensing*, *GE-18*(1), 39–43. doi: 10.1109/TGRS.1980.350258

Jakosky, B. M., Lin, R. P., Grebowsky, J. M., Luhmann, J. G., Mitchell, D. F., Beutelschies, G., ... Zurek, R. (2015, December). The Mars Atmosphere and Volatile Evolution (MAVEN) Mission. *Space Science Reviews*, *195*(1-4), 3–48. doi: 10.1007/s11214-015-0139-x

Kar, J., & Mahajan, K. K. (1987). On the response of ionospheric magnetisation to solar wind dynamic pressure from pioneer venus measurements. *Geophysical Research Letters*, *14*(5), 507-510. doi: 10.1029/GL014i005p00507

Lee, C. O., Hara, T., Halekas, J. S., Thiemann, E., Chamberlin, P., Eparvier, F., ... Jakosky, B. M. (2017, March). MAVEN observations of the solar cycle 24 space weather conditions at Mars. *Journal of Geophysical Research: Space Physics*, *122*(3), 2768–2794. doi: 10.1002/2016JA023495

Luhmann, J. G. (1986, September). The solar wind interaction with Venus. *Space Science Reviews*, *44*(3), 241–306. doi: 10.1007/BF00200818

Luhmann, J. G., & Cravens, T. E. (1991). Magnetic fields in the ionosphere of Venus. *ßr*, *55*, 201–274. doi: 10.1007/BF00177138

Luhmann, J. G., Elphic, R. C., Russell, C. T., Mihalov, J. D., & Wolfe, J. H. (1980, November). Observations of large scale steady magnetic fields in the dayside Venus ionosphere. *Geophysical Research Letters*, *7*(11), 917–920. doi: 10.1029/GL007i011p00917

Luhmann, J. G., Ledvina, S. A., & Russell, C. T. (2004). Induced magnetospheres. *Advances in Space Research*, *33*(11), 1905–1912. doi: 10.1016/j.asr.2003.03.031

Luhmann, J. G., & Russell, C. T. (1983). Magnetic fields in the ionospheric holes of venus: Evidence for an intrinsic field? *Geophysical Research Letters*, *10*(5), 409-411. Retrieved from `https://agupubs.onlinelibrary.wiley.com/doi/abs/10.1029/GL010i005p00409` doi: https://doi.org/10.1029/GL010i005p00409

Luhmann, J. G., Russell, C. T., & Elphic, R. C. (1984). Time scales for the decay of induced large-scale magnetic fields in the venus ionosphere. *Journal of Geophysical Research: Space Physics*, *89*(A1), 362-368. doi: https://doi.org/10.1029/JA089iA01p00362

Luhmann, J. G., Russell, C. T., Scarf, F. L., Brace, L. H., & Knudsen, W. C. (1987). Characteristics of the Marslike limit of the Venus-solar wind interaction. *Journal of Geophysical Research*, *92*(A8), 8545. doi: 10.1029/JA092iA08p08545

Ma, Y., Combi, M. R., Tenishev, V., Shou, Y., & Bougher, S. (2023). The effects of the upper atmosphere and corona on the solar wind interaction with venus. *Journal of Geophysical Research: Space Physics*, *128*(4), e2022JA031239. (e2022JA031239 2022JA031239) doi: https://doi.org/10.1029/2022JA031239

Ma, Y., Toth, G., Nagy, A., Luhmann, J., & Russell, C. (2020). Formation and Evolution of the Large-Scale Magnetic Fields in Venus' Ionosphere: Results From a Three Dimensional Global Multispecies MHD Model. *Geophysical Research Letters*, *47*(11), e2020GL087593. doi: 10.1029/2020GL087593

Ma, Y. J., Fang, X., Nagy, A. F., Russell, C. T., & Toth, G. (2014). Martian ionospheric responses to dynamic pressure enhancements in the solar wind. *J. Geophys. Res.*, *119*(2), 1272–1286. doi: 10.1002/2013JA019402

Ma, Y. J., Russell, C. T., Fang, X., Dong, C. F., Nagy, A. F., Toth, G., ... Jakosky, B. M. (2017). Variations of the Martian plasma environment during the ICME passage on 8 March 2015: A time-dependent MHD study. *J. Geophys. Res.*, *122*(2), 1714–1730. doi: 10.1002/2016JA023402

Morschhauser, A., Lesur, V., & Grott, M. (2014, June). A spherical harmonic model of the lithospheric magnetic field of Mars. *Journal of Geophysical Research: Planets*, *119*(6), 1162–1188. Retrieved 2019-12-04, from `http://doi.wiley.com/10.1002/2013JE004555` doi: 10.1002/2013JE004555

Phillips, J. L., Luhmann, J. G., & Russell, C. T. (1984a). Growth and maintenance of large-scale magnetic fields in the dayside Venus ionosphere. *Journal of Geophysical Research: Space Physics*, *89*(A12), 10676-10684. Retrieved from `https://agupubs-onlinelibrary-wiley-com.proxy.lib.uiowa.edu/doi/abs/10.1029/JA089iA12p10676` doi: 10.1029/JA089iA12p10676

Phillips, J. L., Luhmann, J. G., & Russell, C. T. (1984b). Growth and maintenance of large-scale magnetic fields in the dayside venus ionosphere. *Journal of Geophysical Research: Space Physics*, *89*(A12), 10676-10684. doi: 10.1029/JA089iA12p10676

Ramstad, R. (2020). The global current systems of the Martian induced magnetosphere. *Nature Astronomy*, *4*, 7.

Ruhunusiri, S., Halekas, J. S., Espley, J. R., Eparvier, F., Brain, D., Mazelle, C., ... Jakosky, B. M. (2018). An Artificial Neural Network for Inferring Solar Wind Proxies at Mars. *Geophysical Research Letters*, *45*(20), 10,855–10,865. doi: 10.1029/2018GL079282

Russell, C., Luhmann, J., & Elphic, R. (1983). The properties of the low altitude magnetic belt in the venus ionosphere. *Advances in Space Research*, *2*(10), 13–16.

Russell, C. T., Snare, R. C., Means, J. D., & Elphic, R. C. (1980). Pioneer venus orbiter fluxgate magnetometer. *IEEE Transactions on Geoscience and Remote Sensing*, *GE-18*(1), 32-35. doi: 10.1109/TGRS.1980.350256

Shinagawa, H., & Cravens, T. E. (1988). A one-dimensional multispecies magnetohydrodynamic model of the dayside ionosphere of Venus. *Journal of Geophysical Research*, *93*(A10), 11263. doi: 10.1029/JA093iA10p11263

Shinagawa, H., & Cravens, T. E. (1989, June). A one-dimensional multispecies magnetohydrodynamic model of the dayside ionosphere of Mars. *Journal of Geophysical Research: Space Physics*, *94*(A6), 6506–6516. Retrieved 2019-12-04, from `http://doi.wiley.com/10.1029/JA094iA06p06506` doi: 10.1029/JA094iA06p06506

Sánchez-Cano, B., Narvaez, C., Lester, M., Mendillo, M., Mayyasi, M., Holmstrom, M., ... Durward, S. (2020). Mars' ionopause: A matter of pressures. *Journal of Geophysical Research: Space Physics*, *125*(9), e2020JA028145. doi: https://doi.org/10.1029/2020JA028145

Vignes, D., Mazelle, C., Rme, H., Acuña, M. H., Connerney, J. E. P., Lin, R. P., ... Ness, N. F. (2000). The solar wind interaction with mars: Locations and shapes of the bow shock and the magnetic pile-up boundary from the observations of the mag/er experiment onboard mars global surveyor. *Geophysical Research Letters*, *27*(1), 49-52. doi: https://doi.org/10.1029/1999GL010703

Xu, Q., Xu, X., Zhang, T. L., Rong, Z. J., Wang, M., Wang, J., ... Luo, L. (2021). The Venus Express observation of Venus' induced magnetosphere boundary

at solar maximum. *Astron. Astrophys.*, *652*, A113. doi: 10.1051/0004-6361/202141391

Zhang, M. H. G., & Luhmann, J. G. (1992). Comparisons of peak ionosphere pressures at Mars and Venus with incident solar wind dynamic pressure. *J. Geophys. Res.*, *97*, 1017–1025. doi: 10.1029/91JE02721

Figure 1.

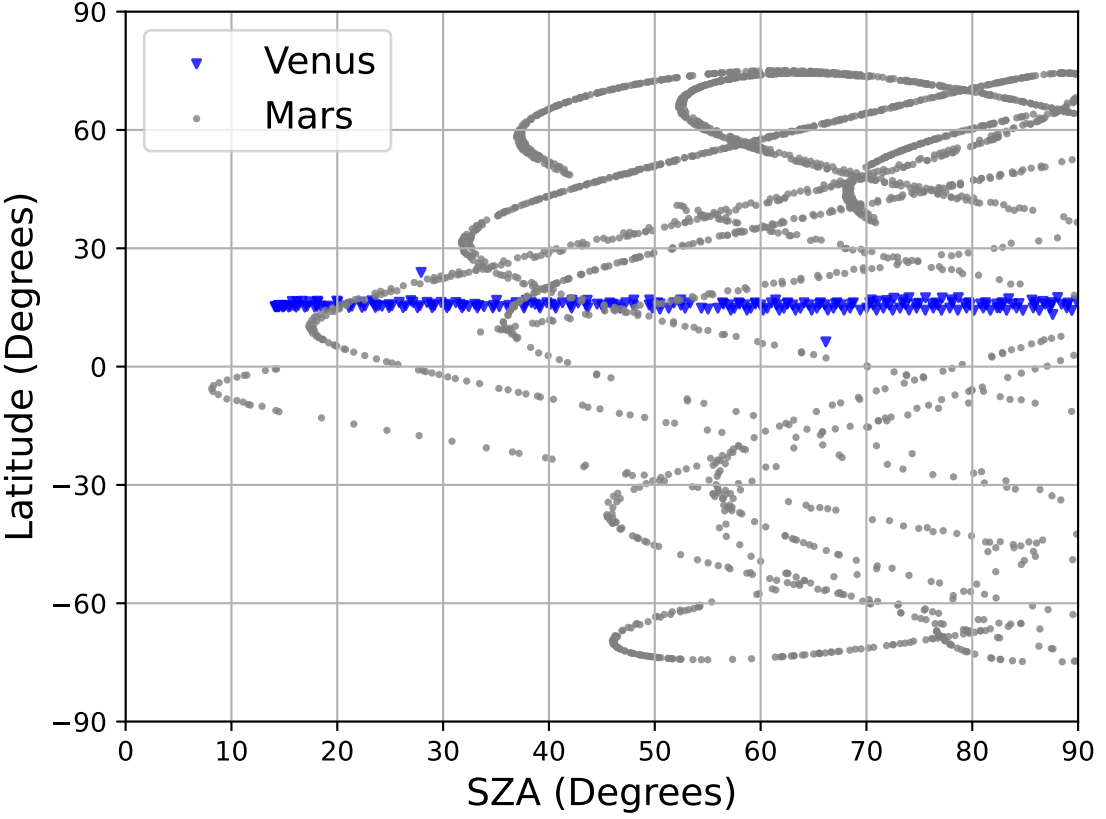
Venus
Mars
Latitude (Degrees)
SZA (Degrees)
90
60
30
0
−30
−60
−90
0
10
20
30
40
50
60
70
80
90

Figure 2.

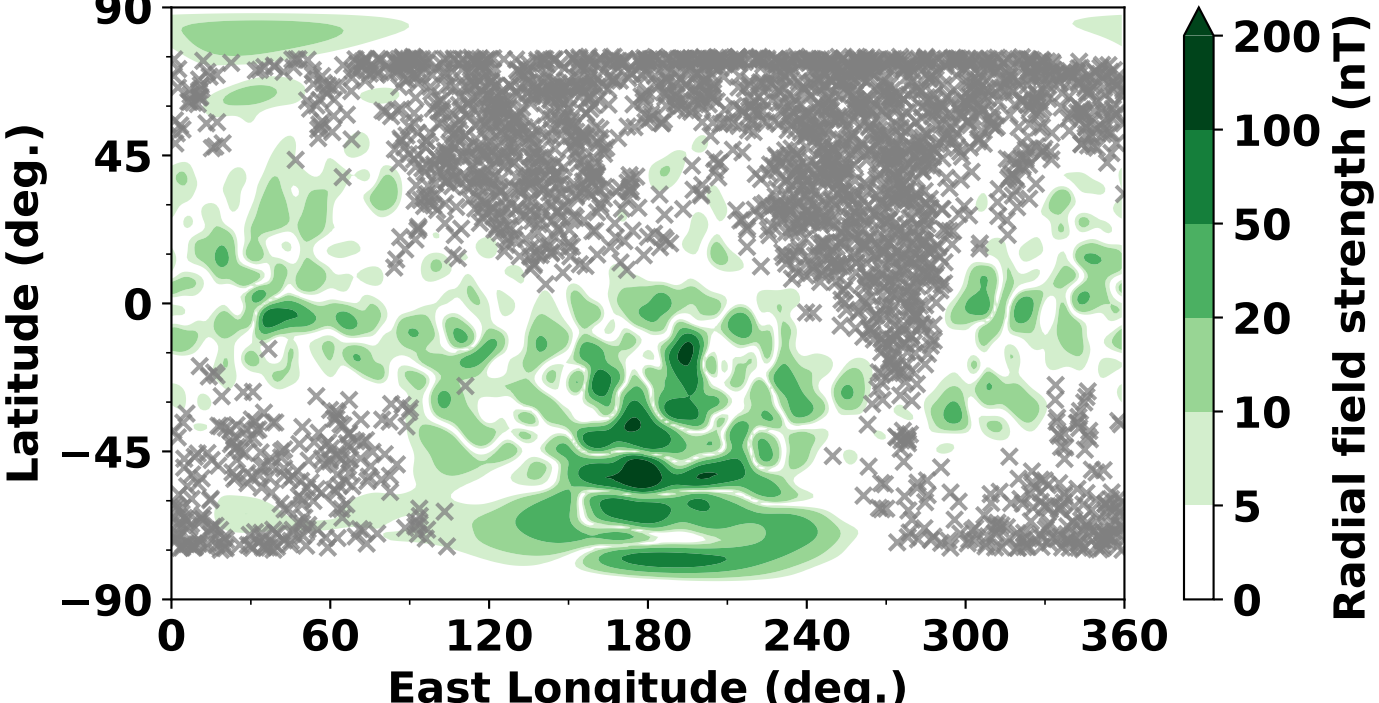
90
45
0
−45
−90
Latitude (deg.)
0
60
120
180
240
300
360
East Longitude (deg.)
200
100
50
20
10
5
0
Radial field strength (nT)

Figure 3.

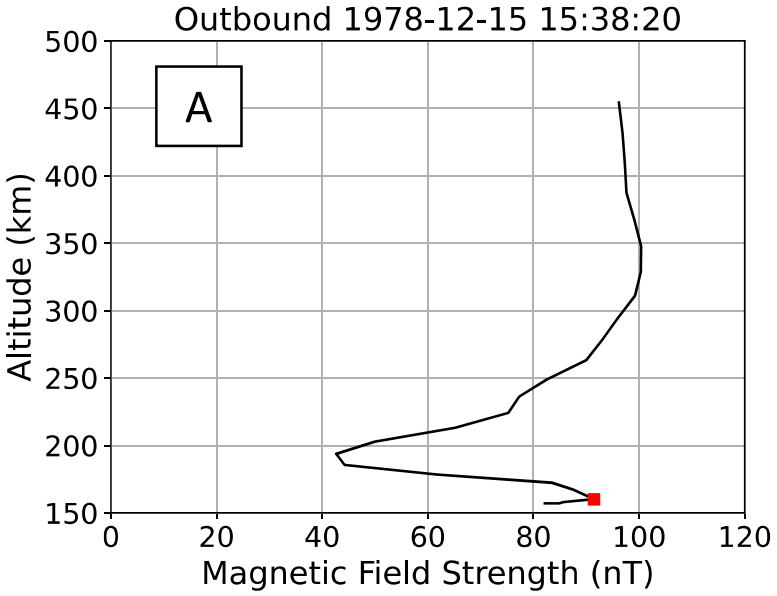
Outbound 1978-12-15 15:38:20
A
Altitude (km)
Magnetic Field Strength (nT)

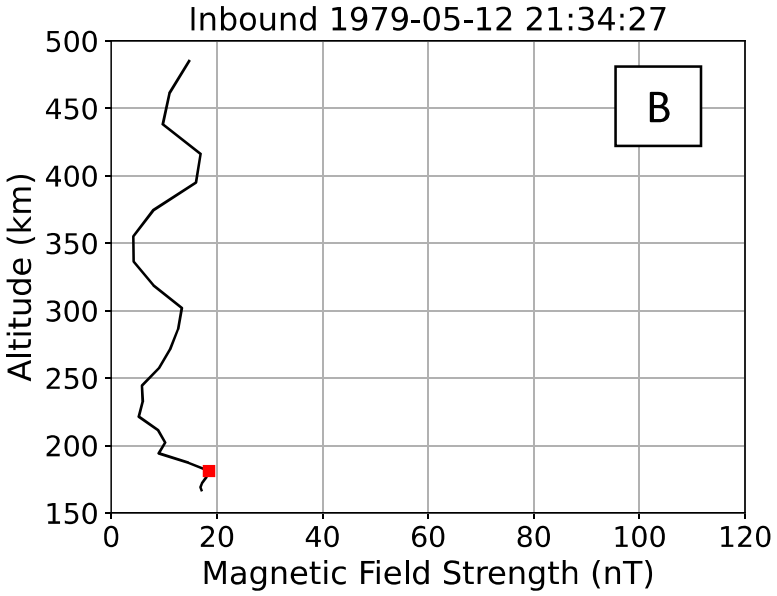
Inbound 1979-05-12 21:34:27
B
Altitude (km)
Magnetic Field Strength (nT)

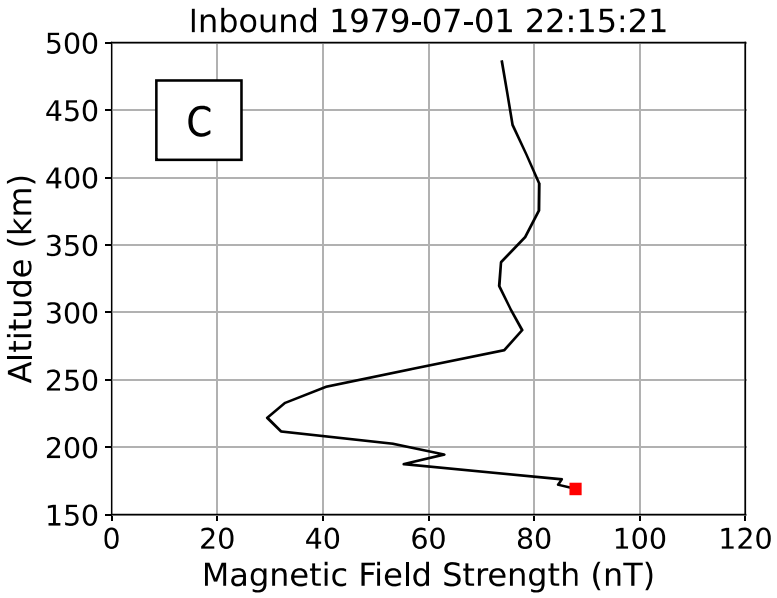
Inbound 1979-07-01 22:15:21
C
Altitude (km)
Magnetic Field Strength (nT)

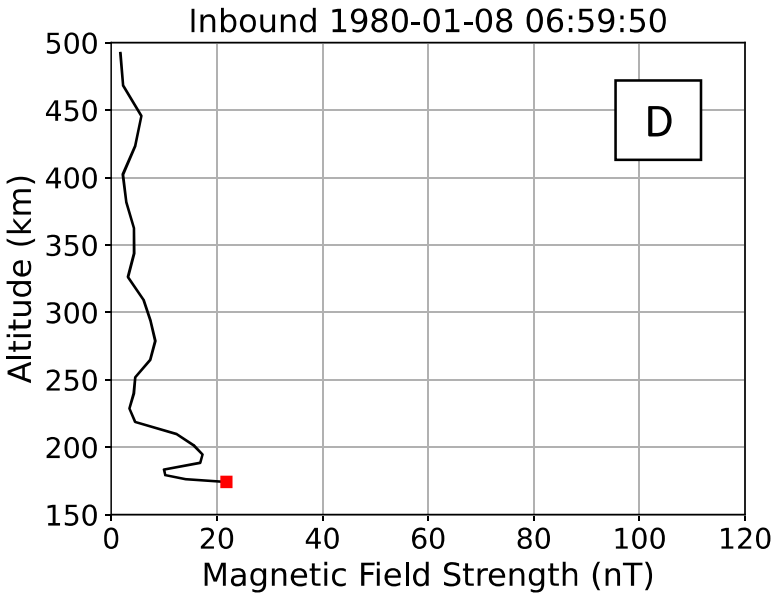
Inbound 1980-01-08 06:59:50
D
Altitude (km)
Magnetic Field Strength (nT)

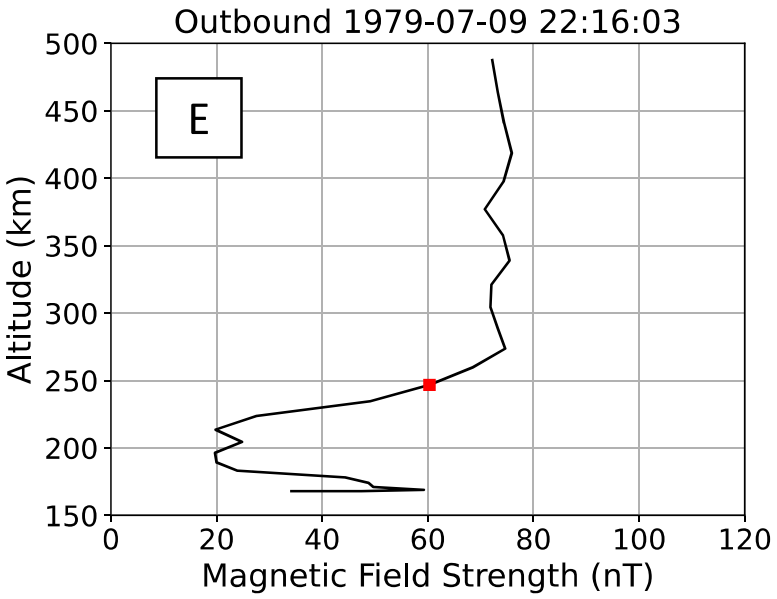
Outbound 1979-07-09 22:16:03
E
Altitude (km)
Magnetic Field Strength (nT)

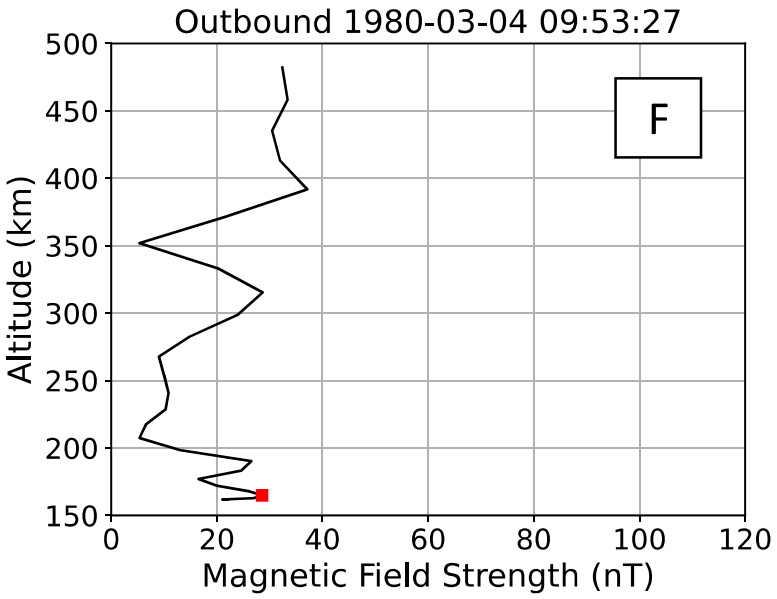
Outbound 1980-03-04 09:53:27
F
Altitude (km)
Magnetic Field Strength (nT)

Figure 4.

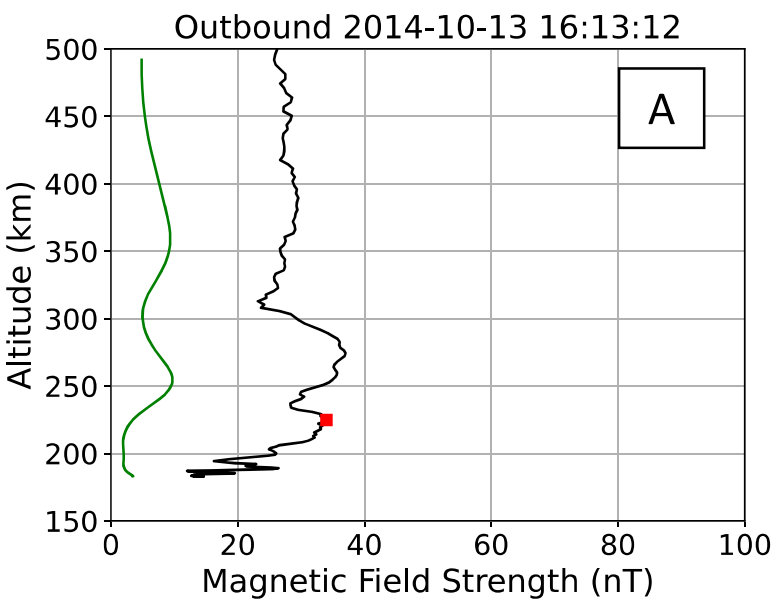
Outbound 2014-10-13 16:13:12
A
Altitude (km)
Magnetic Field Strength (nT)

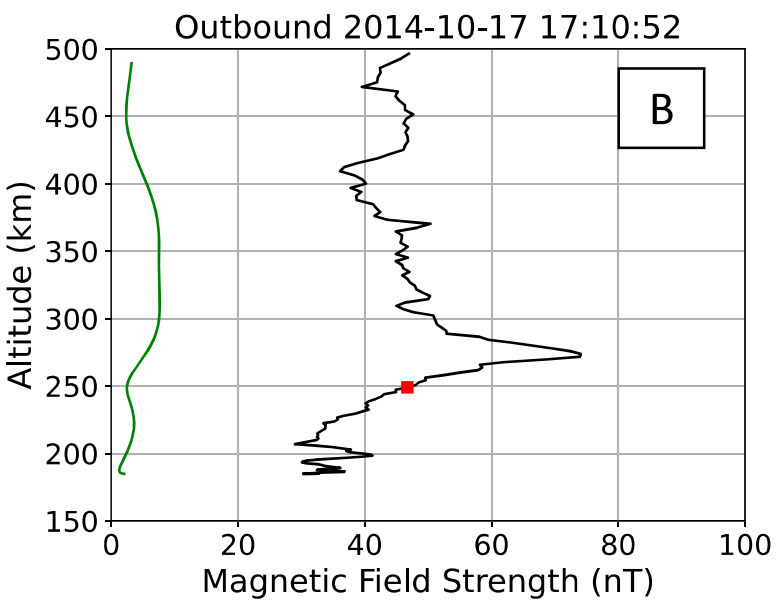
Outbound 2014-10-17 17:10:52
B
Altitude (km)
Magnetic Field Strength (nT)

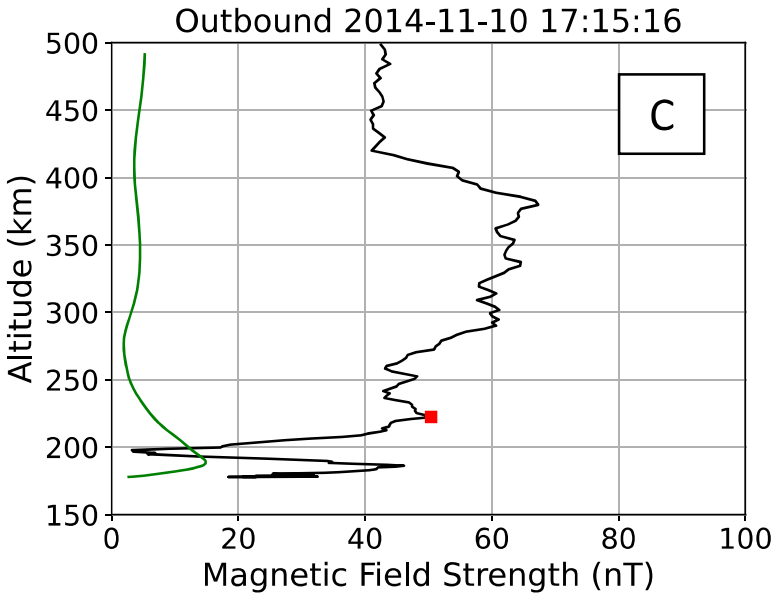
Outbound 2014-11-10 17:15:16
C
Altitude (km)
Magnetic Field Strength (nT)

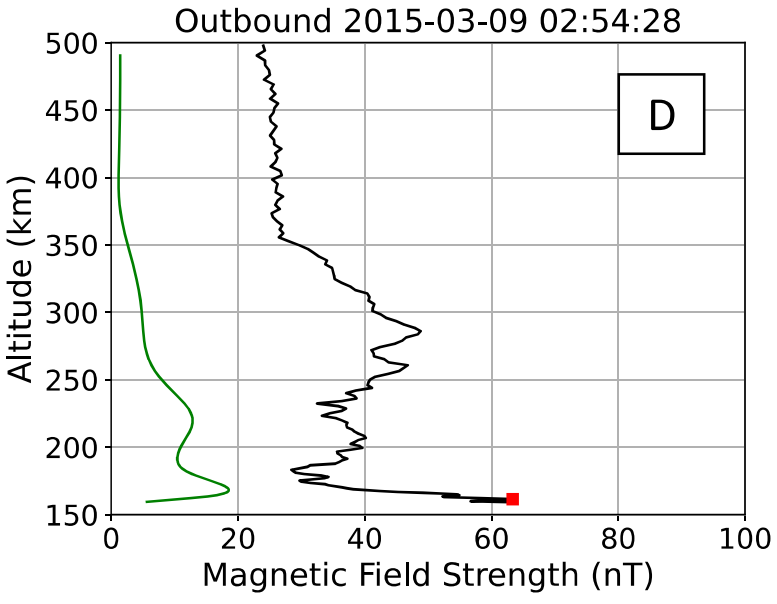
Outbound 2015-03-09 02:54:28
D
Altitude (km)
Magnetic Field Strength (nT)

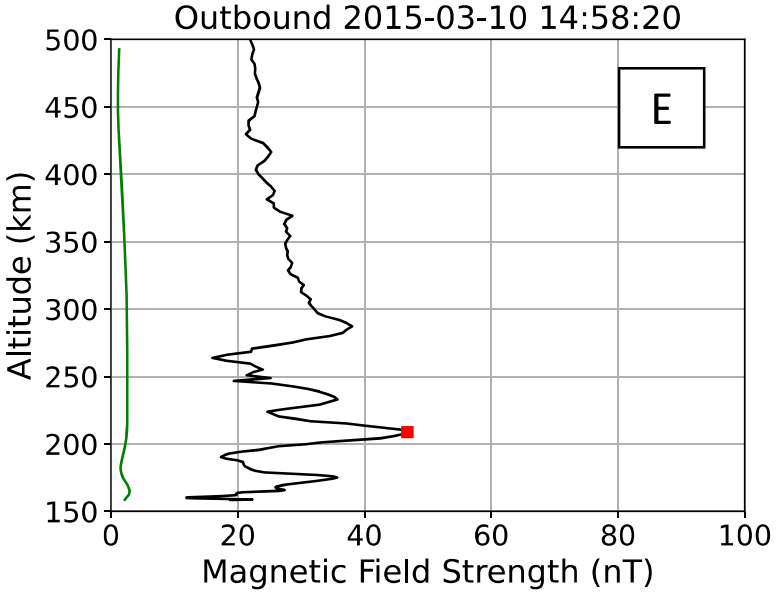
Outbound 2015-03-10 14:58:20
E
Altitude (km)
Magnetic Field Strength (nT)

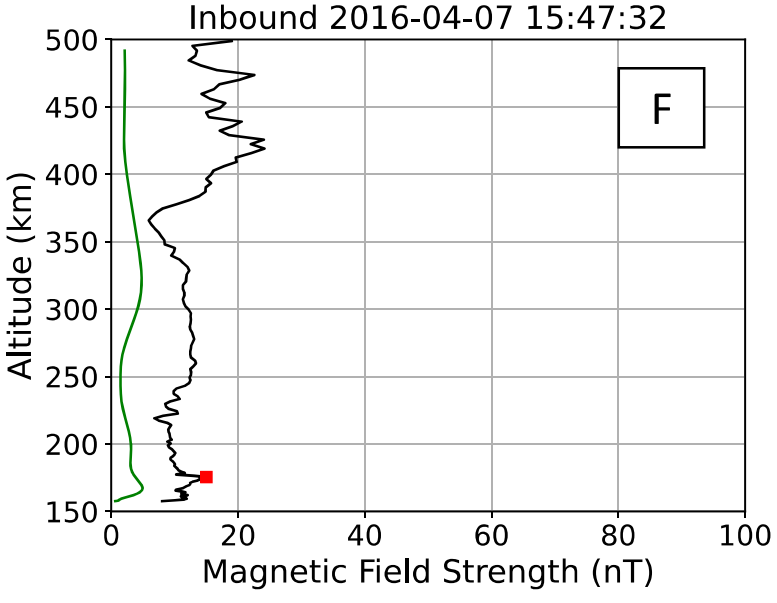
Inbound 2016-04-07 15:47:32
F
Altitude (km)
Magnetic Field Strength (nT)

Figure 5.

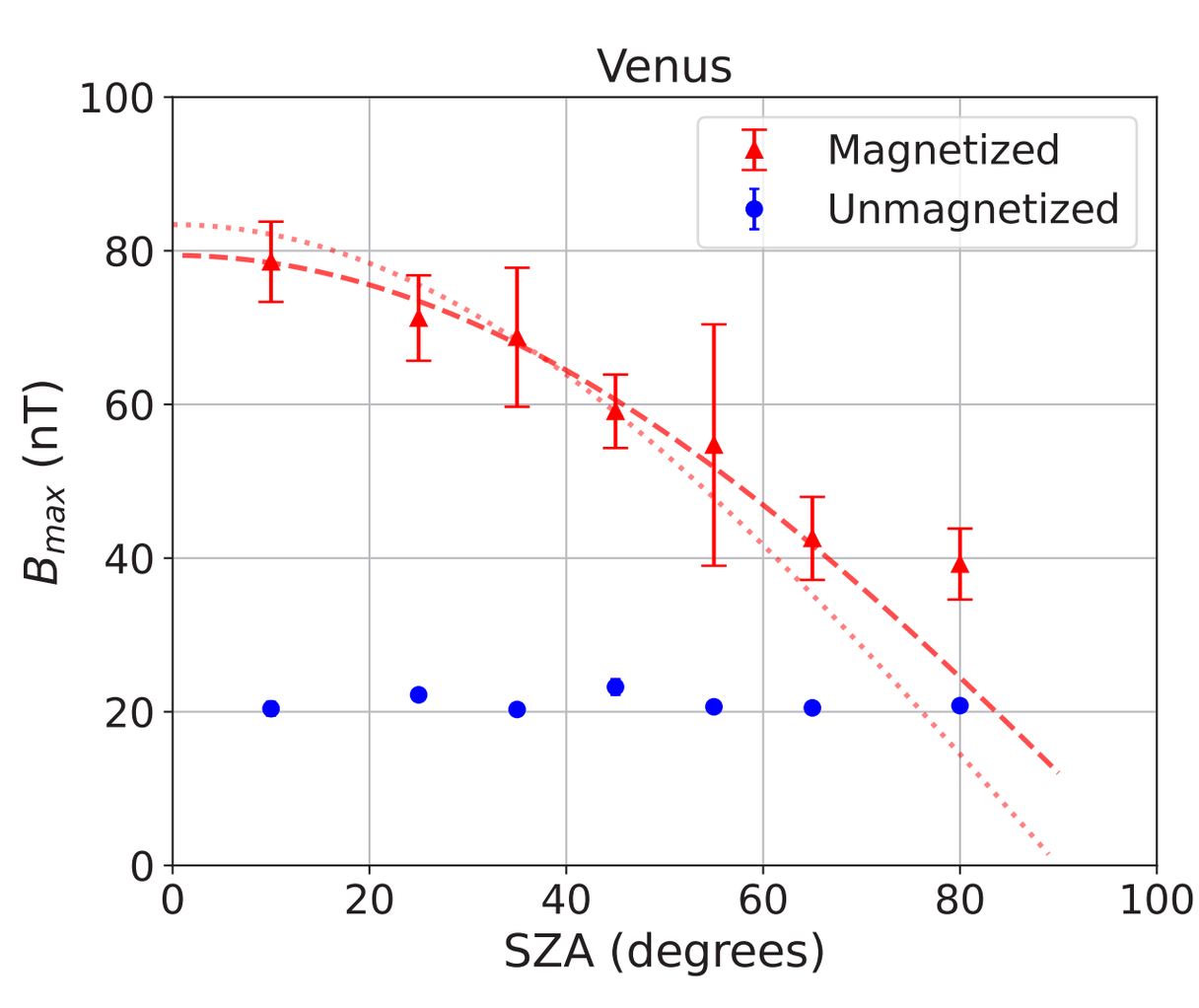
Venus
Magnetized
Unmagnetized
B_{max} (nT)
SZA (degrees)
0
20
40
60
80
100

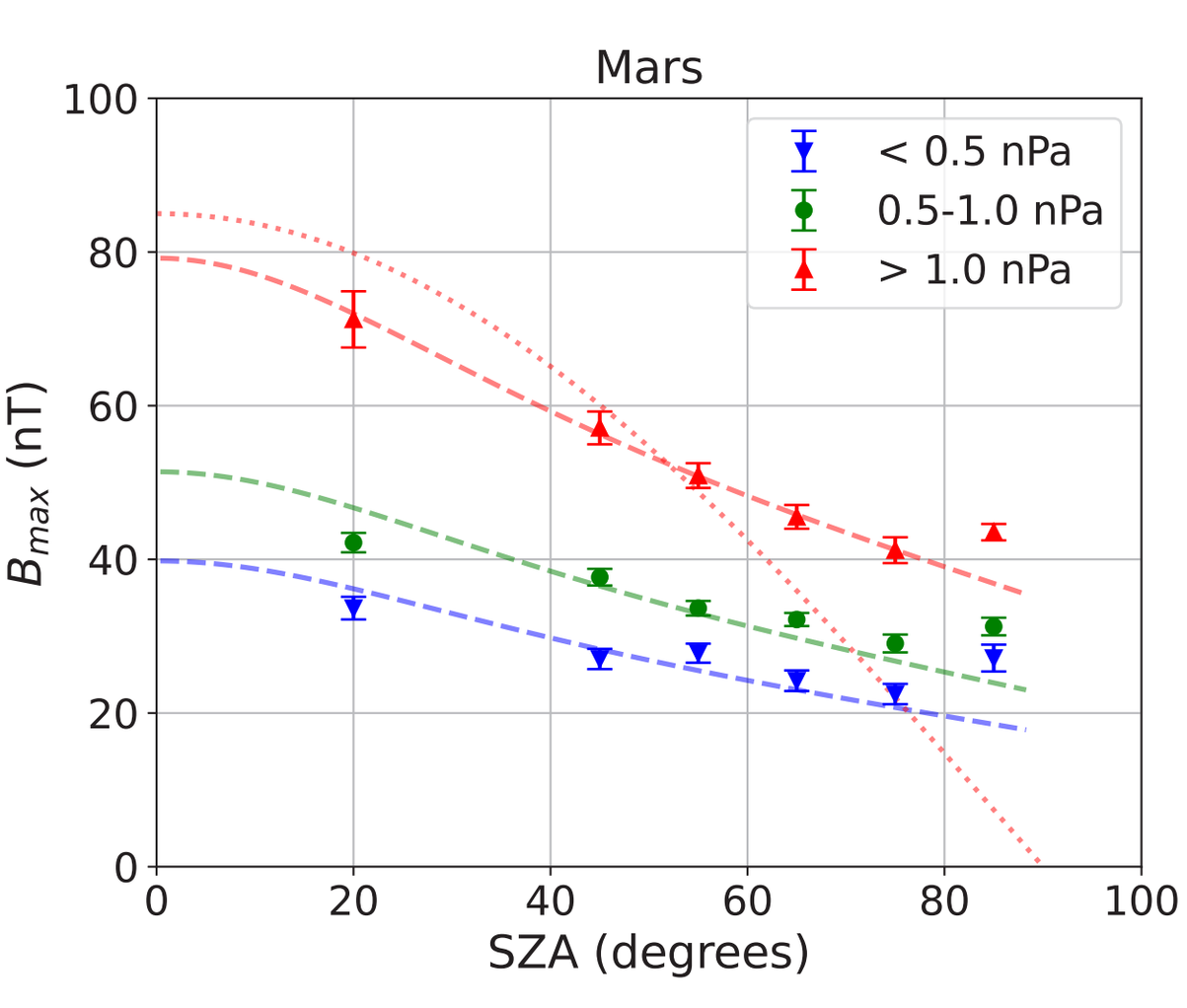
Mars
< 0.5 nPa
0.5-1.0 nPa
> 1.0 nPa
B_{max} (nT)
SZA (degrees)
0
20
40
60
80
100

Figure 6.

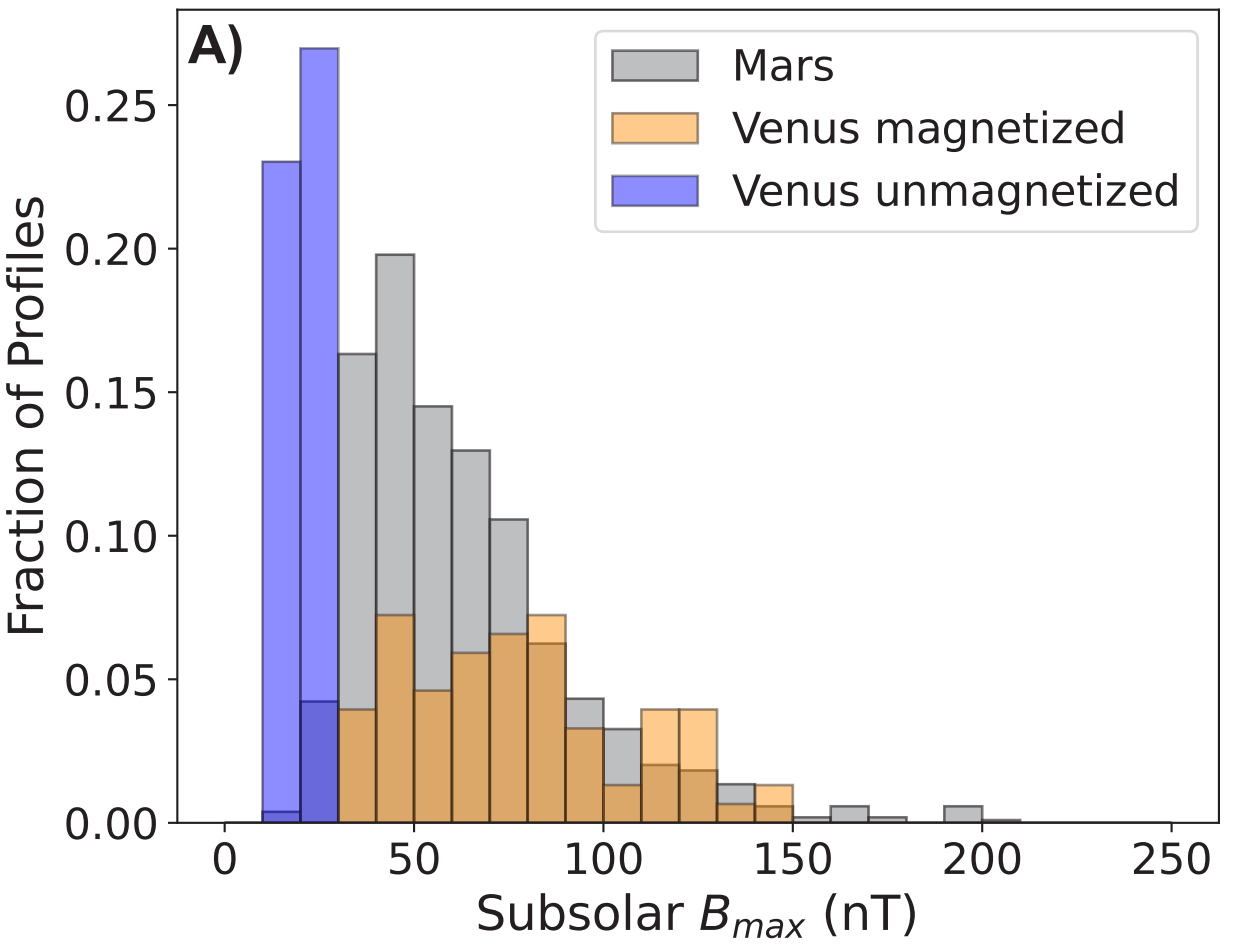
A)
Mars
Venus magnetized
Venus unmagnetized
Fraction of Profiles
0.25
0.20
0.15
0.10
0.05
0.00
0
50
100
150
200
250
Subsolar B_{max} (nT)

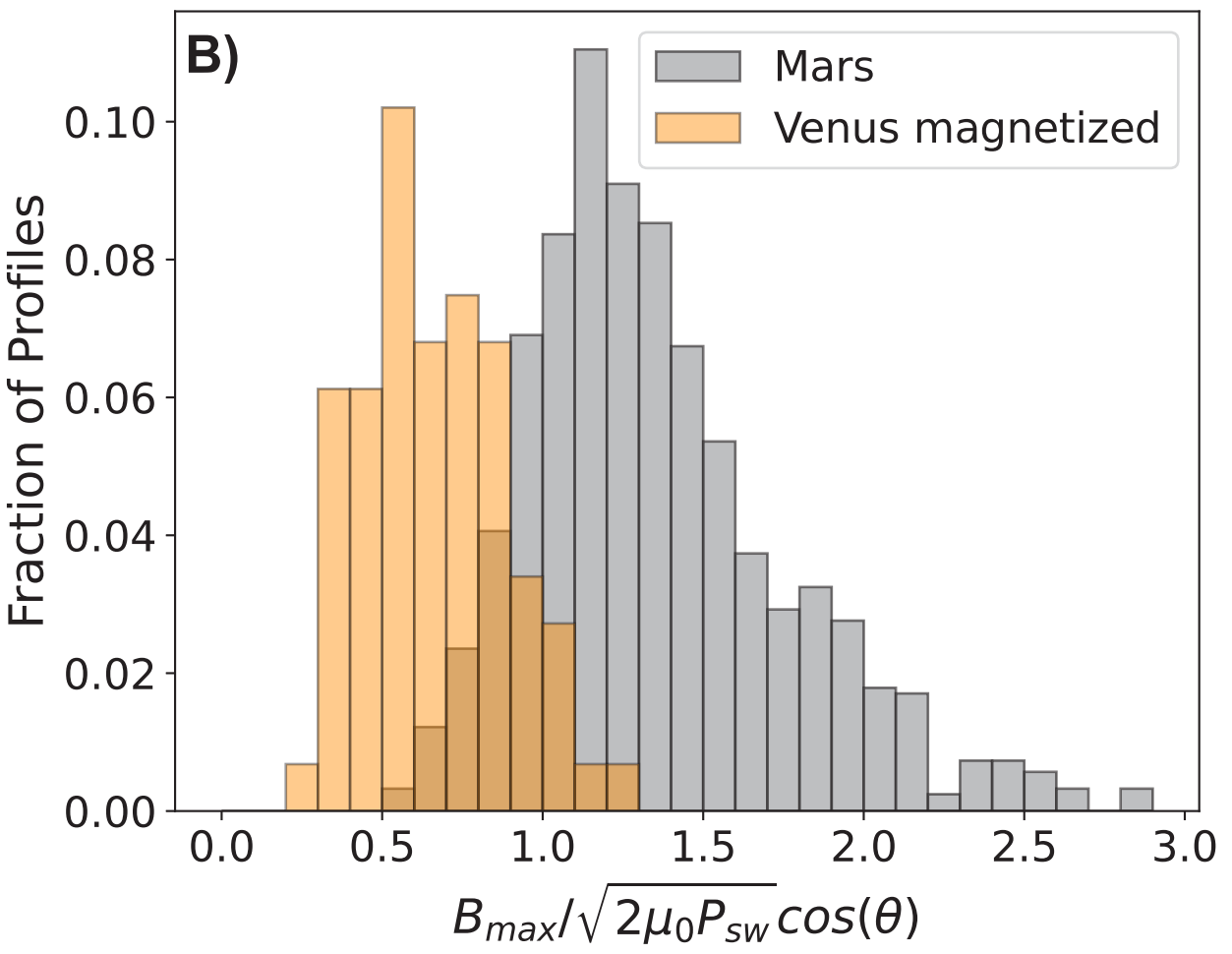
B)
Mars
Venus magnetized
Fraction of Profiles
0.10
0.08
0.06
0.04
0.02
0.00
0.0
0.5
1.0
1.5
2.0
2.5
3.0
$B_{max}/\sqrt{2\mu_0 P_{sw}}cos(\theta)$

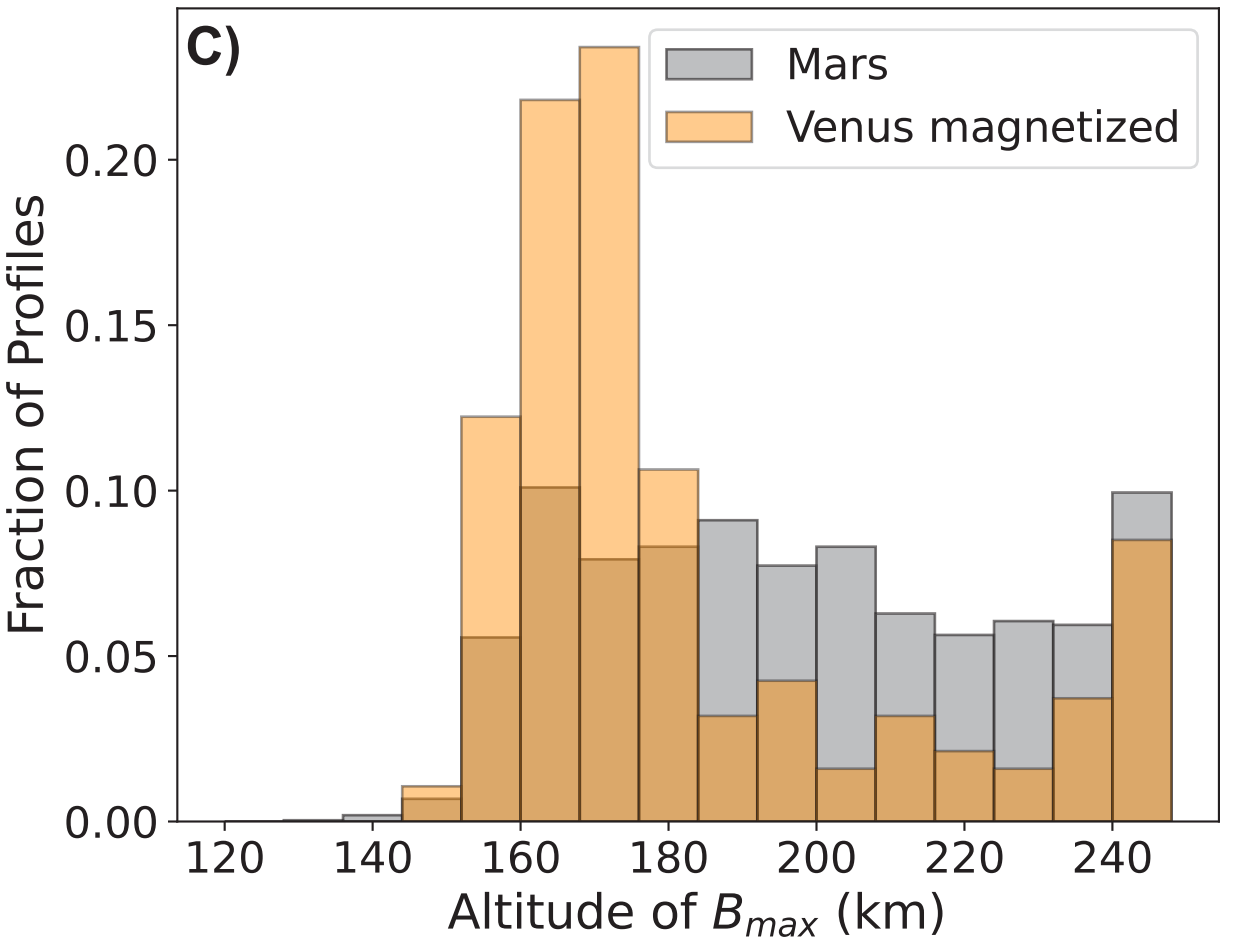
C)
Mars
Venus magnetized
Fraction of Profiles
0.20
0.15
0.10
0.05
0.00
120
140
160
180
200
220
240
Altitude of B_{max} (km)

Figure 7.

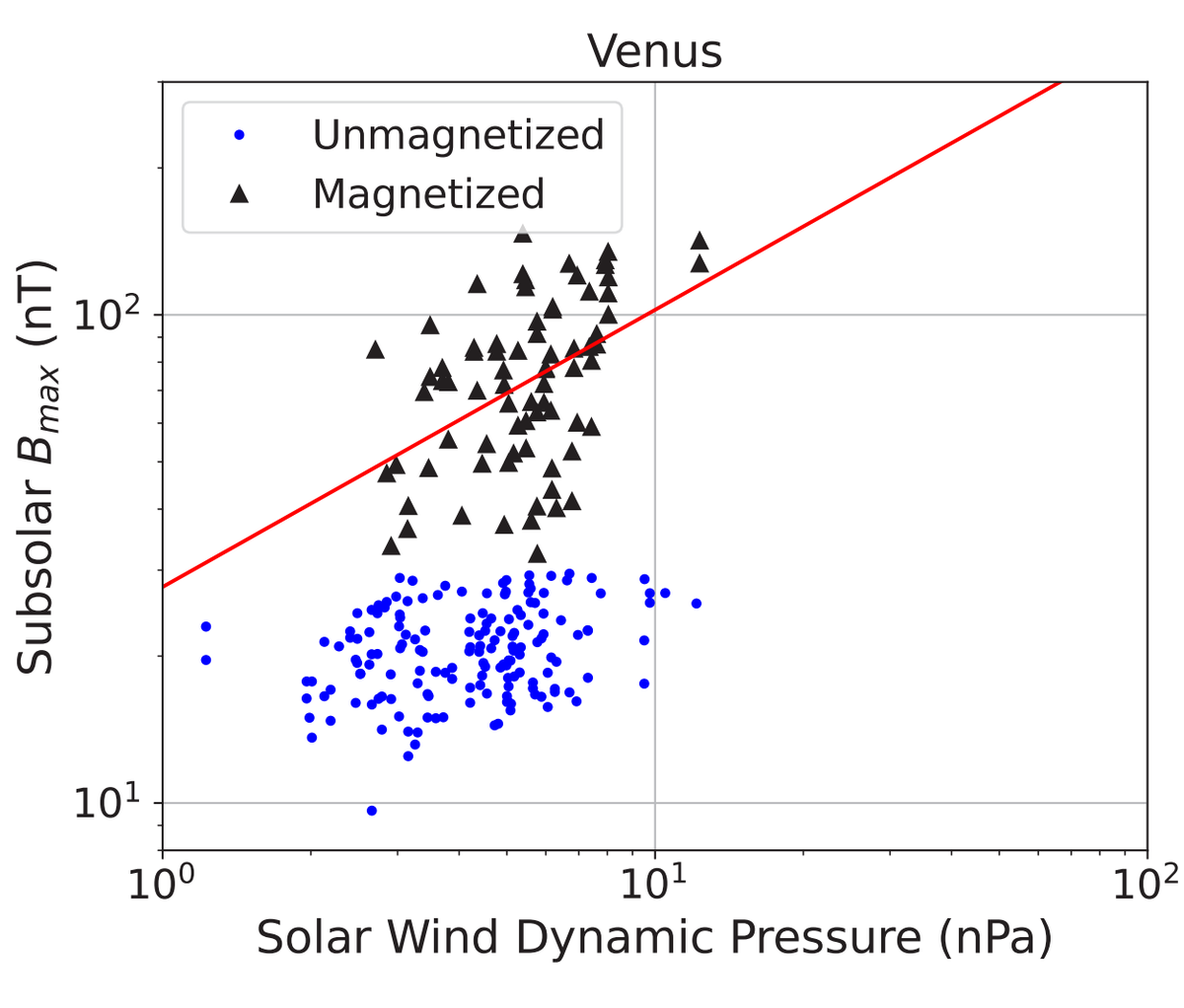
Venus
Unmagnetized
Magnetized
Subsolar B_{max} (nT)
10^2
10^1
10^0
10^1
10^2
Solar Wind Dynamic Pressure (nPa)

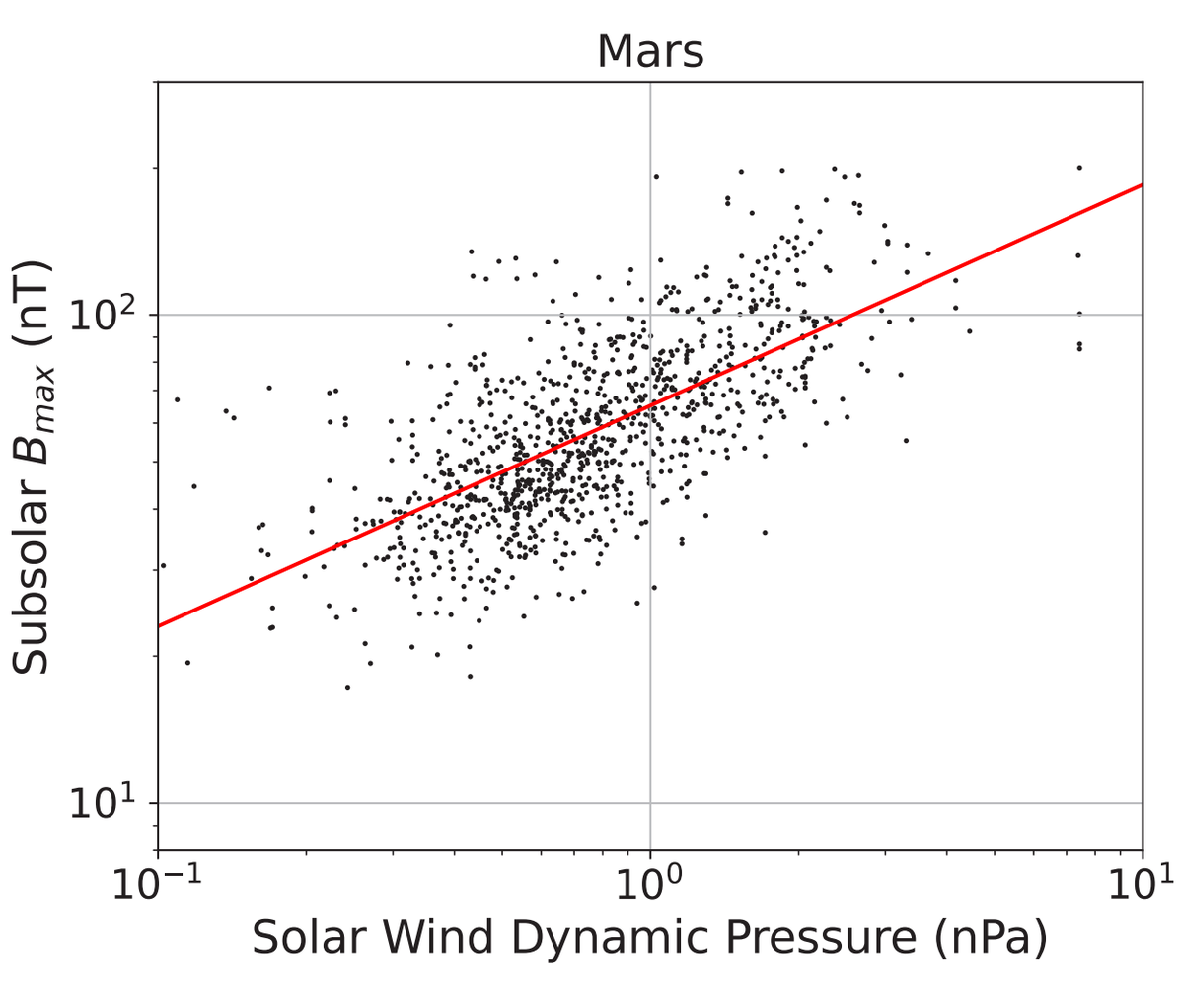
Mars
Subsolar B_{max} (nT)
10^2
10^1
10^{-1}
10^0
10^1
Solar Wind Dynamic Pressure (nPa)